Thesis

Lisa Audenaert

An automotive MIMO radar calibration using targets of opportunity in different weather conditions

TU Delft

Thesis

by

Lisa Audenaert

to obtain the degree of Master of Science
at the Delft University of Technology,
to be defended publicly on Monday December 16, 2019 at 10:00 AM.

Student number: 4152654

Thesis committee:

Prof. dr. A. Yarovoy,	TU Delft, Chairman
Dr. O. A. Krasnov,	TU Delft, Supervisor
Dr. ir. R. F. Remis,	TU Delft, External member
Dr. N. Petrov,	TU Delft, Supervisor

TU Delft

Abstract

For the past few decades the development of self-driving cars has been a large topic in both science and industry. One of the main challenges to be addressed before bringing it to the marker is realisation of sufficiently reliable sensing capabilities in different weather, light and traffic conditions. To realise these features, modern self-driving autos are equipped with cameras, lidars and radars.

Automotive radar has an advantage over other sensors in that it is better at operating in bad weather conditions. To see the extent of the effect that adverse weather conditions might have on the statistics of the data a statistical analysis was performed on real measurement data. During heavy rain there is a shift that can be observed in the Radar Cross Section (RCS) of the target. The average RCS of the target increases slightly when it is raining.

In (Multiple Input Multiple Output) MIMO radar it is important to calibrate the radar system as there can be both amplitude and phase distortions between the channels that can produce measurement errors. Calibration coefficients are usually estimated in a controlled environment with known targets. This calibration however, does not reflect possible degradation of the antenna pattern in the operational mode where the possible presence of dust, water or mud on the bumper might interfere with the radar performance. Instead it might be feasible to estimate this from objects of opportunities that are regularly appearing in the radar field of view.

To tackle this problem a method is used that estimates these calibration coefficients from measurement data. The method needs to know the angle at which the target is located, however the range of the target can remain unknown. It uses the ideal steering vector and one of the antenna elements as a reference element. The method can recreate the phase errors very well, but relies on the reference element for the amplitude estimation. Therefore the performance is based on what element is chosen as a reference. To choose the right reference element some pre-processing is proposed.

The problem of sensor calibration with targets at unknown locations is addressed jointly with simultaneous localisation and mapping (SLAM) of the sensor. This problem is addressed jointly with the modification of an Extended Kalman Filter (EKF) for SLAM. The EKF is used to make an estimate for both the location of the radar, the location of the objects of opportunity and the estimation of the calibration coefficients based of these landmarks at the same time. The performance of the resulting algorithm has been investigated and it is feasible to calibrate the radar while driving in this way.

Contents

1 Introduction **1**
- 1.1 Motivation . . . 1
- 1.2 Literature review . . . 1
- 1.3 Problem statement . . . 3
- 1.4 Outline of thesis . . . 4

2 Radar background **5**
- 2.1 Radar basics . . . 5
  - 2.1.1 Radar range equation . . . 6
  - 2.1.2 FMCW. . . . 7
  - 2.1.3 MIMO radar . . . 7
  - 2.1.4 Radar calibration . . . 9

3 Influence of weather on radar statistics **11**
- 3.1 Description of radar . . . 11
- 3.2 Measurement description . . . 12
- 3.3 Data association . . . 15
- 3.4 Discussion of results . . . 15
  - 3.4.1 Comparison near- and far-field radar beam . . . 16
  - 3.4.2 Weather analysis . . . 16
- 3.5 Conclusion . . . 18

4 Estimating of calibration coefficients **21**
- 4.1 Estimation algorithm with mutual coupling . . . 21
- 4.2 Estimation algorithm without mutual coupling . . . 25
- 4.3 Moving radar . . . 26
- 4.4 Conclusion . . . 27

5 Phase error distribution **29**
- 5.1 Complex normal distribution . . . 29
- 5.2 Phase error distribution . . . 29
- 5.3 Beam-pointing error analysis . . . 30
- 5.4 Combined analytical expression . . . 32
- 5.5 Conclusion . . . 33

6 Joint SLAM and calibration **35**
- 6.1 Theory of SLAM . . . 35
  - 6.1.1 Probabilistic model for SLAM . . . 36
- 6.2 Theory of Extended Kalman Filter . . . 36
- 6.3 Including calibration estimation in EKF-SLAM . . . 37
  - 6.3.1 Probabilistic model used for joint calibration and SLAM . . . 37
  - 6.3.2 Necessary modifications . . . 38
- 6.4 EKF for joint SLAM and calibration . . . 39
  - 6.4.1 State vector . . . 39
  - 6.4.2 Prediction step . . . 40
  - 6.4.3 Correction step . . . 41
  - 6.4.4 Jacobian H . . . 42
  - 6.4.5 Problem with implementation for uncalibrated array . . . 44

6.5 Target initialisation . . . 45
6.5.1 Phase array estimation . . . 45
6.5.2 Doppler beam sharpening . . . 46
6.5.3 Combined estimator . . . 49
6.6 Images from algorithm . . . 49
6.6.1 Wrong angle . . . 50
6.7 Verification of the combined estimation . . . 51
6.8 Conclusion . . . 53

7 Conclusion **55**
7.1 Conclusion . . . 55
7.2 Future research . . . 56

A Equations for Extended Kalman Filter **59**
A.1 Partial derivatives of Jacobian H . . . 59
A.1.1 r . . . 59
A.1.2 v . . . 59
A.1.3 gamma . . . 60

Bibliography **63**

1 Introduction

1.1. Motivation

For many years now car manufacturers have been implementing increasingly complex automotive radars in their cars as they can offer many benefits to the driver. They are very popular and become commonplace in most modern vehicles. Automotive radar sensors can detect and track objects. They offer the driver assistance through adaptive cruise control assistance, parking assistance and collision avoidance. This and other applications can be seen in Figure 1.1.

Most of these features are safety related and in the future these sensors will even be implemented to create fully automated vehicles. As time goes on we are becoming more reliant on these aids to assist us with driving. This is especially the case when there are adverse weather conditions or road conditions that might impede the safety of the driver. This makes it very important for these automotive radars to be robust and to work reliably in all types of difficult road situations.

The road and weather condition will be constantly changing and there are other factors such as age of the sensor that might impact the working of the sensor. Radar calibration can be used to counter some of this decaying, but in the ideal case this would happen continuously while the radar is driving. Therefore it is necessary to find targets while driving that the radar might be calibrated upon. These target will also be called targets of opportunity that appear in the vision of the radar while driving.

All of this stresses that it is important to study all situations that might occur on the road and that might affect the performance of these types of radars and even improve upon the performance through calibration. The problem is a large one and encompasses a lot of topics. This thesis looks at two different topics that can affect the performance of the radar. Firstly a study of the effect of adverse weather conditions on the statistical data of a commercial available radar and secondly a method for estimating the calibration coefficients of a Multiple Input and Multiple Output (MIMO) radar in its operational mode on the road.

The goal will be to increase the performance of the radar in operating conditions and with the data that is already available in the radar. This increased performance will make it safer for drivers on the road and make the radar systems more reliable in all type of weather situations.

1.2. Literature review

Weather

Looking at how radar behaves in adverse weather conditions we can find that automotive radar is less affected by them than other types of sensors like lidar [25] and this is one of the reasons it is so popular. It is however not unaffected and it will be interesting to see if the effects of weather will affect the statistics of the radar.

Statistical analysis of the data available from a Continental radar in different weather conditions. This is Frequency Modulated Continuous Wave (FMCW) radar that operates at

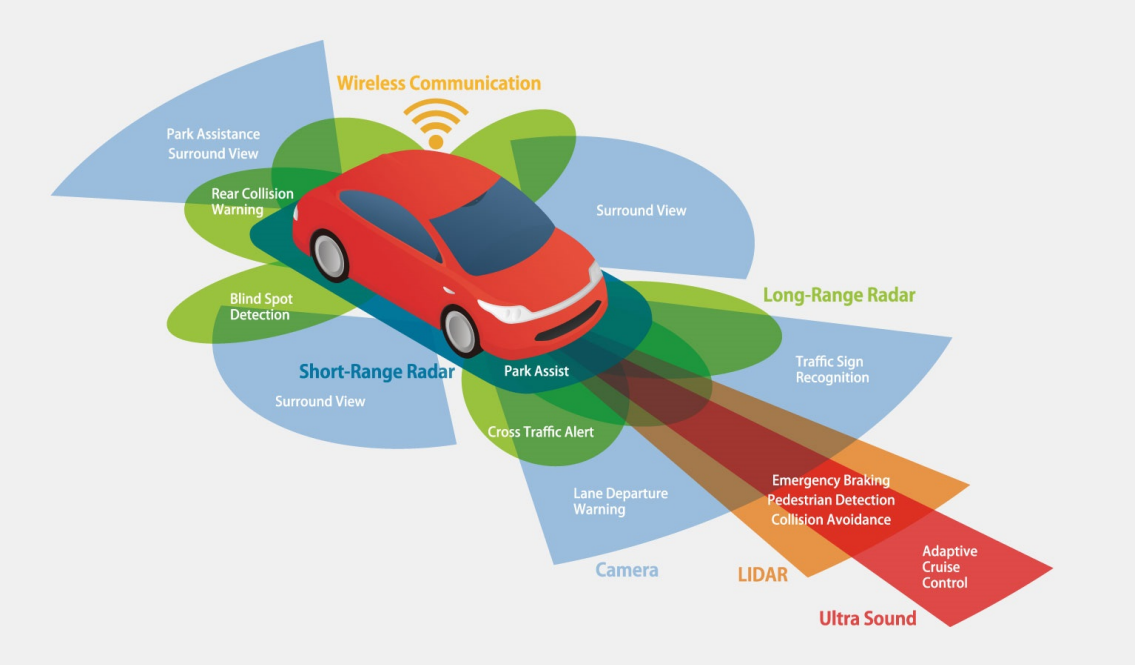

Figure 1.1: Automotive radar application

$77GHz$. This radar outputs a vectorised data file which has only a few parameters available. The literature was focused on one of these: the Radar Cross Section (RCS) of the target. This is the main focus as this one has the most potential of all the parameters outputted by the radar.

RCS attenuation due to the propagation through rain is usually discussed in dB/km and is described in an ITU recommendation [34]. However this does not necessarily mean it is also valid in the small ranges that are used in automotive radar. On such a small range there can be a lot more sources that influence this.

According to [23] there is no discernible change between the RCS of a dry and a wet reflector. They measured the backscatter of the reflector after wetting the surface of it and compared it to the radar return of a dry reflector and saw no significant changes.

Another study in this area [7] depicts a minimal loss where the water sheet thickness on the reflector is ”relatively thin” (<0.25mm for 17.8GHz). This shows that there can be some variation due to the rain.

However most papers agree that the largest influence on attenuation is in the effect of a wet radome or a water film on the radome. There have been a number of studies [8] [15] that look into this. So where wetting the reflector appears to not have much influence the influence of a water layer is substantial. When there is a large enough water or ice layer it can even fully block the function of the automotive radar and distort the antenna pattern.

Another path that might prove useful is to look at [19], [27] and [13]. They represent papers that show the different scattering behaviours of several different road surfaces in different weather conditions. It shows that the surface of the road is important for the level of backscatter and that the backscatter can increase drastically on wet concrete.

Nowadays all radars are made by specialised companies, like Continental and Bosch, who have their own version that they bring on the market. The companies process the raw radar data and only output a vectorised data file. On one hand this makes the radar very consumer friendly, however on the other hand it also causes the radar to behave like a black box. It performs processing on the raw data internally and outputs only a list of detected objects and some of the characteristics of these objects. It is however not known in what way this alters the statistical effects that might be observed with the radar data.

MIMO

After this analysis the topic will shift to estimating the calibration coefficients for a MIMO radar. In MIMO several similar antennas that are located closely to each other are combined to create a better signal. Every antenna element that is produced has its own imperfections and therefore it is necessary to calibrate the antenna array to compensate for the faults that are always present. These errors are caused by imperfect channels and the non-uniformity of the array. They are detected and estimated during the calibration of the array; a process which is usually performed by measuring a predefined set of targets while the car is standing still. This process is time-consuming and very precise.

Inaccurately estimating these coefficients will degrade the performance of the array so therefore there have been a number of implementations on how to estimate the calibration coefficients. After the measurement data has been received by the receiver it is range processed into bins with a (Fast) Fourier Transform. Most of the calibration algorithms work with the range processed signal.

When the initial calibration is done this does not mean that the process of calibration is finished now. This is because there are a lot of factors that could change the array's response over time: like the age of the components, rough environment, thermal effects and so on. Therefore it remains necessary to keep calibrating the array over time. Next to the road there are certain distinct objects that periodically appear when driving. This can be either a road sign or a lamp post and they should always give roughly the same detection distribution to the radar. The measurements of these objects could be used to recalibrate the radar.

The paper [14] talks about the errors that can occur and what effect they have on the calibration. The negative effects that are described are: beam pointing error, broadening of the main beam, a rise in the sidelobes or the deviation of the grain of the antenna array.

It also proposes a self-calibration method that, to find the amplitudes, calculates the mean over all signal amplitudes which allows to estimate the gain of each transmitter and receiver combination by $\hat{A}_{mn} = |\tilde{x}_{mn}|/|\bar{x}|$. For the phase errors it assumes a linear behaviour as they should be located in the far-field. A least squares method is used for determining the phase errors.

In our application it will be necessary to use real measurement data for the estimation of the calibration coefficients and there are already certain papers that have this requirement. There are however certain requirements that are needed for doing this.

Most methods like [31] require a very precise measurement scenario where all of the reference sources and their locations need to be known beforehand. A lot of papers extended on [31], giving different implementations for different types of sensors however these papers all have a quite rigid set of requirements.

In paper [22] the requirements are relaxed as they jointly try to estimate the coupling matrix, the element factor and the phase centre. There are no more requirements on the location of the array centre or about the individual antenna elements. The trade-off for this relaxation of the requirements is that the algorithm is very complex and does not always converge (quickly).

In [28] a method is proposed for estimating the MIMO calibration matrix from real measurement data that only needs the angle of the target to be known. It relies on the ideal signal steering vector that can be created from the angles to reproduce the antenna pattern. The method "arbitrarily fixes the phases of the entries of the first antenna element to the phases of the measured signals". By doing this it alleviates the need to estimate the absolute phase term in the first element. The method relies on the first element to be able to relate to the measured signals.

1.3. Problem statement

This thesis is divided into two subtopics that are both looking at different parts of the plethora of factors that might impede the performance of the radar.

Firstly it will study the effect of rain and other adverse weather conditions on the statistics of observed radar targets. To do this there will be a statistical analysis of real radar data that

has been collected in different weather conditions.

Secondly it will try to use objects of opportunity to estimate the calibration coefficients of a MIMO radar system. To do this it will be necessary to look at different algorithms that can be used to estimate the calibration coefficients. As well as a way to simulate and calculate the radar moving through the environment while calculating the calibration coefficients. It will also be necessary to study the impact of calibration error on the radar measurement.

1.4. Outline of thesis

The rest of this thesis is organised as follows.

- Chapter 2 will provide with the background information and the state-of-the-art research in the field. It will give an overview of how general radar systems function as well as more information about MIMO radar and its calibration. There is also information on SLAM and the EKF that will be important later.
- Chapter 3 will take a look at the influences of adverse weather conditions on the radar data. To do this there will be a description of the used radar and target setup and of the algorithm used to process the available data.
- Chapter 4 will then look into how the calibration coefficients can be estimated and how accurate those estimations will be.
- Chapter 5 will take a look at the beam pointing error and how this can be related to distributions in phase or magnitude error of calibration matrix. The relation between these errors will be used further in Chapter 6.
- Chapter 6 will describe the algorithm of SLAM as it is described in literature. Then the joint problem of simultaneous localisation, calibration and mapping is then addressed with the modification of EKF SLAM. The performance and limitations of the proposed algorithm are investigated via numerical simulations.
- The final chapter discusses all of the results in the earlier chapters and draws conclusions from this. It also gives some recommendations for potential future research.

2

Radar background

The word radar stands for **RA**dio **D**etection **A**nd **R**anging. As the name suggest the systems uses radio waves to both detect objects and determine the object's range. It was invented during the Second World War, but it has been improved upon since then and now has become much more advanced. In the modern day radar can be used to determine the range, angle and velocity of targets all at once.

This upcoming chapter will give an overview of how general radar systems function as well as more information about MIMO radar and radar calibration [24] [30]..

2.1. Radar basics

Radar is a detection system that uses electromagnetic (EM) waves to determine the location of objects by studying the reflections of the EM waves on these objects. The range R can be determined by the time it takes for these waves to propagate to the target and back (ΔT). Here $c \approx 3 * 10^8$ is the speed of light in m/s.

$$\delta R = \frac{c\Delta T}{2} \tag{2.1}$$

This the the theoretical limit, but this is in fact a statistical parameter and this is why we would need to take a look at the Cramer-Rao Lower Bound (CRLB). This bound limits the variance of any unbiased estimator $\hat{\theta}$ and it can be defined in the following way [17] [18]:

$$var(\hat{\theta} \geq \frac{1}{-E\left[\frac{\partial^2 lnp(\boldsymbol{x};\theta)}{\partial\theta^2}\right]} \tag{2.2}$$

Now looking into how the range can be approximated using this equation [17]:

$$var(\hat{R}) \geq \frac{(\delta R)^2}{SNR\bar{F^2}} \tag{2.3}$$

Here the value $\bar{F^2}$ is related to the bandwidth of the target and it can be assumed a constant. We can see that this equation is related to the range resolution and the SNR of the target. This statistical estimation will always be less than the range resolution.

When the detected object is moving there will be a change in the frequency of the reflected waves (Δf). This is called the Doppler effect and it can be used to determine the velocity of the detected object relative to the velocity of the radar (Δv).

$$\Delta f = \frac{2\Delta v}{c} \tag{2.4}$$

Every object has a different way of scattering or reflecting EM waves and this is represented by the Radar Cross Section (RCS) σ. The RCS is for example influenced by the size and the material of the target. The higher the RCS the better the object is detectable by the radar.

The targets of interests are assumed to be lamp posts and these can be fairly well represented as a point like target. However at certain angles and ranges they might not be and they will be spread out over several bins. Then they are considered to be an extended target instead. On the roof most of the targets that were studied were extended targets. That means that they have multiple reflective surfaces that can be grouped together to form one extended object. An extended target is an object of interest that appears in multiple resolution bins. The range resolution of a radar can be defined as the minimal distance at which two different target can be distinguished. That means that they are at least a beamwidth apart. The beamwidth is usually defined as the angular distance between the half power points. This is at -3dB from the peak of the main lobe.

Similar to the range resolution we can also define the Doppler resolution; which is the smallest difference in Doppler shift for a moving target that can be detected. Positive Doppler shifts usually indicate that the target is moving towards the radar while negative shifts indicated it is moving away from it.

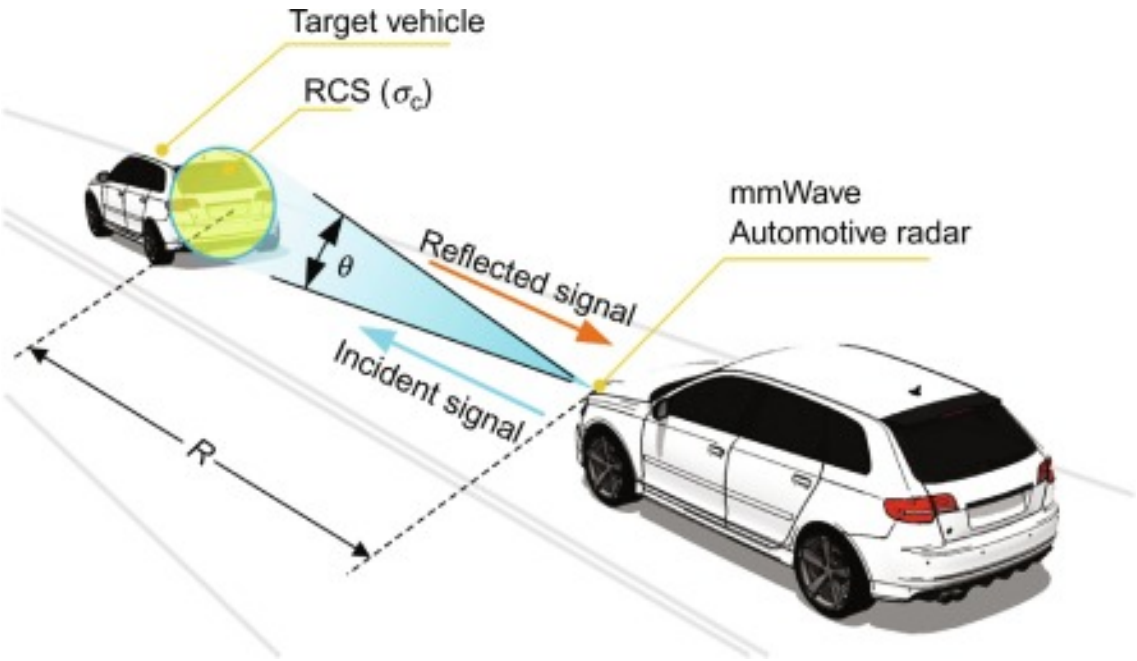

Figure 2.1: Automotive radar principle, Figure taken from [1]

The resolution of the velocity δv can be described in this way:

$$\delta v = \frac{\lambda}{2T} \tag{2.5}$$

Here T is the radar refresh rate
The beamwidth can be approximately described as:

$$\delta \phi \approx \frac{\lambda}{D} \tag{2.6}$$

Here D is the size of the antenna array.

2.1.1. Radar range equation

The radar performance can be described by the radar range equation which ties a lot of the radar's characteristics together.

$$P_r = \frac{P_t \lambda^2 G_t G_r \sigma}{(4\pi)^3 R^4} \tag{2.7}$$

Here P_r represents the power of the received signal and it depends on the transmitted power P_t, the wavelength λ, the gain of both the transmitting and receiving antennas G_t, G_r, the radar cross section σ and the range R to the target.

2.1.2. FMCW

Frequency Modulated Continuous Wave (FMCW) radar is a type of radar that is constantly emitting and receiving waves that are modulated in frequency. This is very different to a pulsed radar which sends short pulses and determines distance by measuring time delay between the pulses. The advantage is that it is very easy to filter out large stationary objects and slow moving clutter from the received signals.

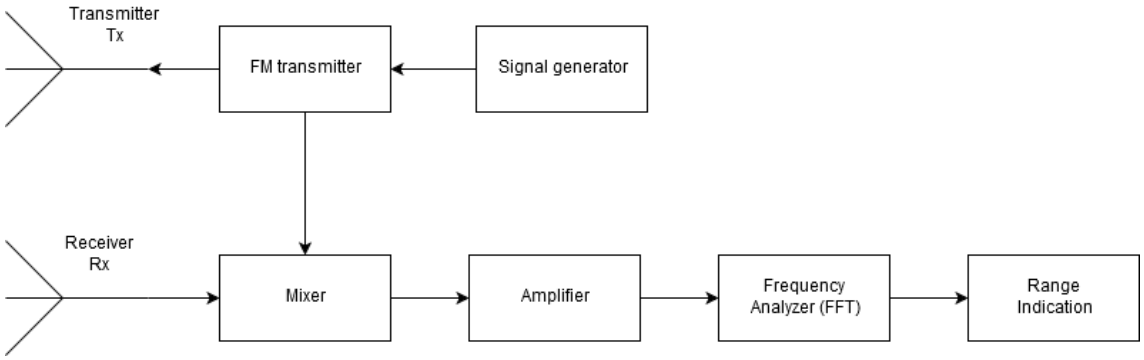

Figure 2.2: Radar block diagram

The signals emitted by the FMCW radar are constantly varying in frequency and the distance to the target is estimated based on the difference in frequency of the transmitted and received signal. A radar block scheme for FMCW radar can be found in Figure 2.2.

Exactly how the waves are modulated can vary between radars, but there are several standard modulation patterns like sawtooth or triangular modulation that are often used. They each have their own advantages and applications.

2.1.3. MIMO radar

In coherent MIMO the transmit and receive antennas are closely located and the signals are coherently combined to improve angular resolution. MIMO uses multiple M transmit T_x and N receive R_x antennas in a priori known formation. The elements are at distance d located from each other.

The signal that are sent must be orthogonal to each other, because otherwise they might start interfering with each other: either constructively or destructively. The orthogonality of the system can be achieved in different ways by for example with spreading them out in time (Time-Division Multiplexing) or frequency (Orthogonal Frequency Division Multiplexing). When the transmitted signals are orthogonal we can create a virtual MIMO array that consists of $M * N$ elements. This virtual array is the advantage that MIMO has over normal phased array as it can have the same performance with less actual antenna elements. This leads to an overall better angular resolution.

The transmit antennas T_x emit a signal $s(t)$ that is reflected on an unknown target at distance r and angle θ of the radar. The distances d between the antennas can be no smaller than $\lambda/2$ to be able to uniquely estimate the angle of arrival θ.

The signal model for MIMO that is written down here was also described in [20].

The transmit signal s_T that is send to a target can be written as:

$$\boldsymbol{s_T}(m) = \sum_{m=1}^{M} e^{-j2\pi f_0 \tau_m(\theta)} x_m(n) = \boldsymbol{a^*(\theta)x}(n), n = 1 \dots N \tag{2.8}$$

where f_0 is the carrier frequency of the radar, $\tau_m(\theta)$ is the time needed by the signal emitted via the mth transmit antenna to arrive at the target, $.^*$ shows the conjugate transpose and N denotes the number of samples of each transmitted signal pulse.

$\boldsymbol{x}(n)$ is the vector of the transmitted signals in all channels and $\boldsymbol{a(\theta)}$ denotes the complex amplitudes of these signals.

$$\boldsymbol{x}(n) = [x_1(n)x_2(n) \dots x_M(n)]^T \tag{2.9}$$

$$\boldsymbol{a(\theta)} = [e^{j2\pi f_0 \tau_1(\theta)}, e^{j2\pi f_0 \tau_2(\theta)}, \dots e^{j2\pi f_0 \tau_M(\theta)}]^T \tag{2.10}$$

The same can be defined for the receiver side where $\boldsymbol{y}(n)$ is the vector of all signals received by the receiver antennas and $\boldsymbol{b(\theta)}$ is the complex amplitudes of these signals. Here $\tilde{\tau}_m(\theta)$ is the time needed for the reflected signal to travel from the target at angle θ to the receiver antenna.

$$\boldsymbol{y}(n) = [y_1(n)y_2(n) \dots y_M(n)]^T \tag{2.11}$$

$$\boldsymbol{b(\theta)} = [e^{j2\pi f_0 \tilde{\tau}_1(\theta)} e^{j2\pi f_0 \tilde{\tau}_2(\theta)} \dots e^{j2\pi f_0 \tilde{\tau}_M(\theta)}]^T \tag{2.12}$$

This leads to the received data vector:

$$\boldsymbol{y}(n) = \sum_{k=1}^{K} \beta_k \boldsymbol{b}^c(\theta_k)\boldsymbol{a}^*(\theta_k)\boldsymbol{x}(n) + \boldsymbol{e}(n), n = 1 \dots N \tag{2.13}$$

where K is the number of targets that reflect the signals back to the radar receiver, β_k are complex amplitudes proportional to the radar cross sections (RCS) of those targets, θ_k are the target location parameters, e(n) denotes the interference plus-noise term, and $(.)^c$ denotes the complex conjugate.

The signals that fall onto the target are reflected back to the radar and received by the R_x antennas. The reflected waves each arrive at the receiver elements at different time instances. This causes them to have a different delay which can be used to estimate the angle of arrival.

The signals that are send by the antennas have to be narrowband ($B << f_c$) to assume that the signal delay can be represented by a phase shift.

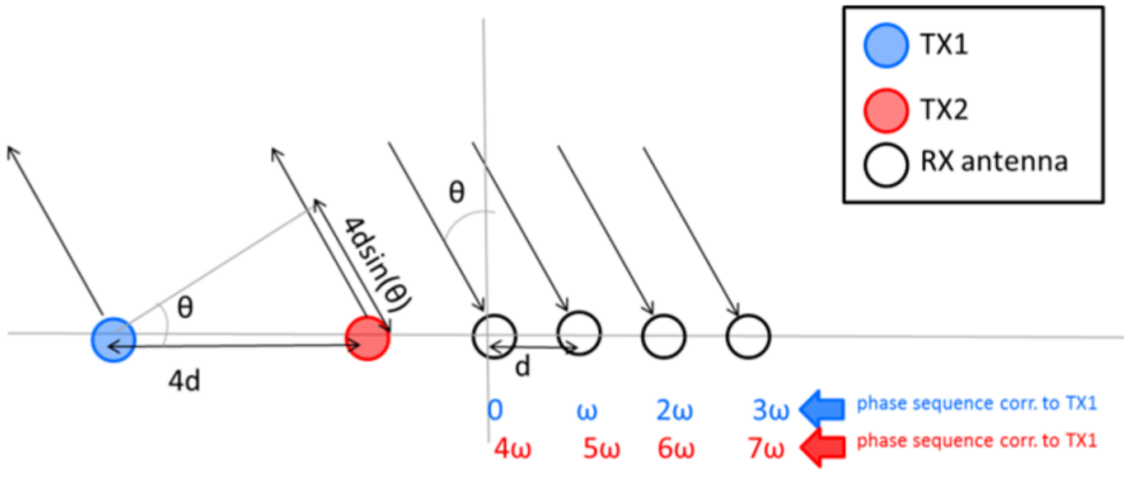

Figure 2.3: MIMO radar principle; Figure taken from [26]

As an example in Figure 2.3 there are two transmit antennas and four receivers. Because the second antenna is placed at a distance of $4d$ any signal will see an additional phase shift of 4ω. This will result in 8 distinct phase sequences at the receiver. The size of the virtual array is 8, and will give the same result as a system with one transmitter and eight receivers. This is called antenna diversity.

2.1.4. Radar calibration

To some degree there are always deviations from the ideal antenna pattern when implementing the antenna elements. These disturbances can cause distortions in the antenna beam pattern like an increase of the side lobe level or they can lower the accuracy of the direction of arrival estimation. The distortions are usually represented in the coupling matrix C, where C is a linear distortion of the true multi-channel signal:

$$\mathrm{s_m}(t,\theta) = \mathrm{C}(\theta)\mathrm{s_0}(t,\theta) \tag{2.14}$$

The calibration consist of estimating the calibration matrix T that reverses the effects done by the coupling matrix C so that:

$$\mathrm{TC}(\theta)\mathrm{s_0}(t,\theta) = \mathrm{s_m}(t,\theta) \tag{2.15}$$

In the ideal case $T = C^{-1}$. When there are M antenna elements the matrices C and T will be of size MxM.

There are two types of error here. The first one is a calibration error that represents the uncertainty in the actual channel gains and phases of the system. When there is no distortion all of the antenna elements behave equally. In this case the elements of the diagonal of the coupling matrix should be all ones. Secondly an error is introduced because the antennas are located so closely together. The transmit antennas will have a direct line-of-sight to the receiver antennas. This will cause interference for the reflected signal. This is also called mutual coupling between the elements.

An initial calibration of the radar will usually be performed just after production. According to[21] the errors that occur after this can be assumed random and uncorrelated. As other systematic errors (which would be correlated) have to be corrected in this first calibration. This makes it possible to approach the problem in a statistical way.

3

Influence of weather on radar statistics

This chapter will look at the influence that the weather has on the radar data itself. For this purpose some measurements were collected with a commercial FMCW radar. The commercial radar has a fixed amount of parameters available for each detected target. All of the measurements were done using the fixed radar scene with set of stationary targets on the roof of the EEMCS building in different weather conditions. The goal was to see the effect of varying weather conditions, especially the presence of precipitation and fog, on the radar data.

3.1. Description of radar

To better understand the way vectorised radar data could be used to assess the influence of weather on the sensor data we first need to analyse what data are available at the output radar interface.

All available data were collected using a Continental ARS-309 radar [9] [10] . This is a Frequency Modulated Continuous Wave (FMCW) based radar with an operating frequency between 76 and 77 GHz. The operating frequency is automatically chosen by the radar. The amount of samples outputted by the radar is between 14 and 16 per second.

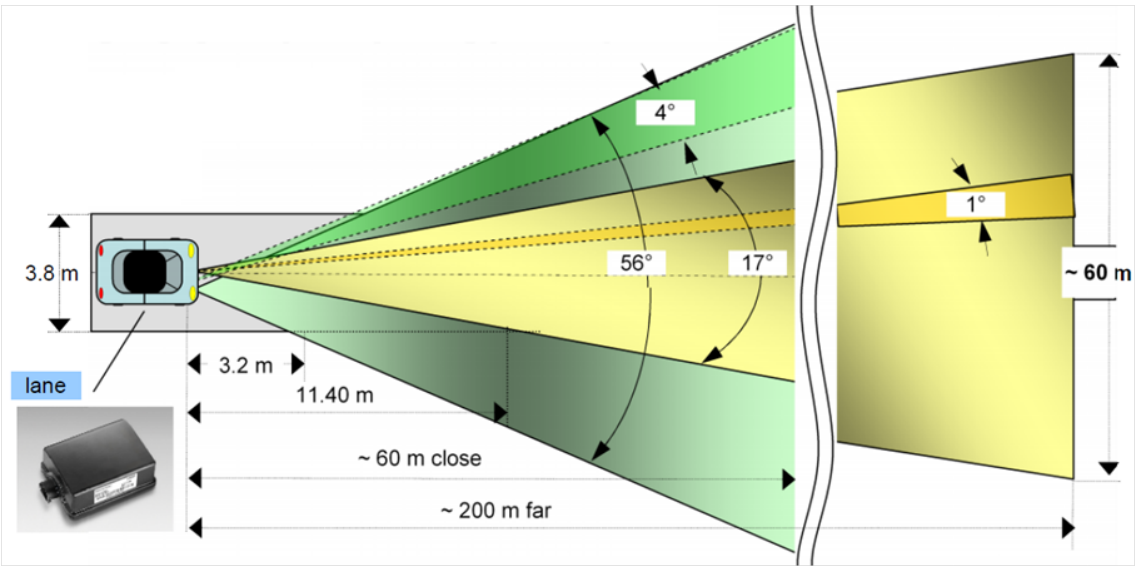

Figure 3.1: Continental radar with two different beams, Figure taken from [10]

It has two radar beams that have very different performances, which makes it difficult to compare the beams directly. The main differences are reproduced in Table 3.1. The mea-

	Near field radar beam	Far field radar beam
Distance range	0.25...60m	0.25...200m
Distance resolution	2m or >5.5 km/h	
Distance accuracy	0.25m or 1.5 @>1m	
Angle resolution	4°close-up range	1°far field
Angle accuracy	1...2°close-up range	0.1°far field

Table 3.1: Continental radar beam performance

surements with the radar haven been taken in a so called stand-still mode. When the radar detects that it is standing still (not moving), it lowers the maximum detection range for near and far field radar beams to 25 and 50 meters, respectively. This was the case in all of the collected measurements.

Variable	Unit
Number of targets	-
Distance (range)	m
Angle (azimuth)	°
Radar Cross Section σ	dBsm2
Length of target	m
Width of target	m
Relative velocity V_{rel}	m/s
Standard deviation V_{rel}	m/s

Table 3.2: Available variables at the output interface of the radar

The radar output consists of only a few variables that are chosen by the manufacturer. Exactly what signal processing algorithms and operations are done to achieve these results is unclear as there are no available detail documentation or access to raw radar data. The list of available at the output interface of the radar variables can be found in table 3.2.

Of note here is that, for stationary targets, the standard deviation of the relative velocity is always equals to 0.01. This is within the accuracy of the measured velocity, but the radar's processing algorithm always assumes that it is moving and that objects are also moving. This might cause the radar to have more difficulty detecting and tracking stationary targets (compared to detecting moving objects). The radar has the possibility to track targets through iterations of sequential scans and to assign a type to them, but for the measurements in this study has been used only detection mode when radar reported only the list of detected targets with measured parameters from the table 3.2.

3.2. Measurement description

The dataset was gathered in a setup on the roof of the EEMCS building. Within this setup the radar measured the antennas and various (mostly metal) objects that are located on the roof. Some of these objects of opportunity can be seen in Figure 3.2. In total there are 18 usable measurements that have been conducted throughout a period of a one year. While working on this project, a few updated measurements were added to this database with an easily identifiable cylindrical reflector that was placed right in front of the radar.

The analysis of the measurements shows that for the same target a variation in the RCS between the two radar beams (near-field and far-field) can be up to 5 dBsm2. The same can be said for the angle as there can be a variation of up to 5 degrees for an extended target. However, there is no such variation observed for the range of the target variable. The spread in observed angles is always larger than the spread in observed range. This is most likely due to the way that extended targets are being processed over multiple 2D range-azimuth angle resolution bins. The accuracy of both near- and far-field radar beams are different and this causes some targets to be assigned to different radar 2D resolution bins. All of these things make it not trivial to make a comparison between radar scene measurements with two sequential near- and far-field antenna beams.

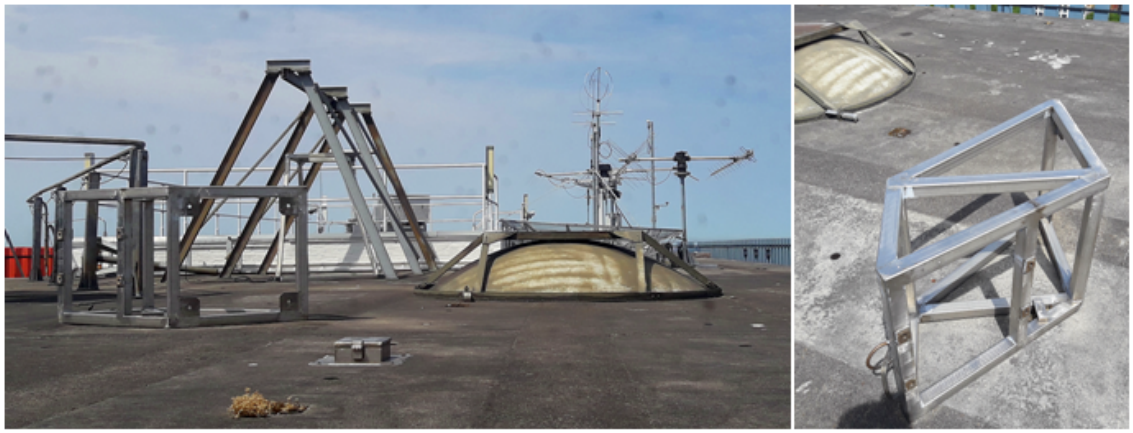

Figure 3.2: Objects of opportunities on roof

To overcome this difficulty it was decided to analyse the influence of the precipitation and for on observed targets parameters for near-field and for far-field beams separately. It is interesting and important to see from the data analysis that the effect of the rain on the observed targets parameters can be detected in both beams. All following results are consistent and can be reproduced for both beams, but only results for the near-field radar beam will be presented in this thesis.

The measurements on the roof were not supported with simultaneous and co-located measurements of visibility. To try to quantify the precipitation intensity during the measurements the logs of the weather station that is located on the same roof was consulted. However, linking the radar measurements with the weather logs show that there were no measurable rainfalls detected in the weather logs during all cases of radar observations. Either the weather logs were inaccurate for the exact situation at the time of the rainfall on the roof or the rain was mild enough that there was no registered by the weather station rainfall rate. As result, collected radar data have only qualitative vague weather condition descriptions (like ”fog”, ”light rain”, ”snow”), that describe the situation in which the measurement was taken. There was however no actual indication of how severe the rain was (other than ”light rain” in some cases).

The datasheet of the radar [10] says that there should be “no impairment of technical data relevant to functionality during rain up to 10 mm/h or fog.” This is all information that is included in the datasheet of the radar about the effect that adverse weather conditions might have. This might be accurate, but it is difficult to verify this statement exactly with the available datasets as there was no exact pluviometer next to it. It proved very difficult to distinguish the measurements with the ’light rain’ tag from the ’normal weather’ cases and this could indicate that the rainfall was less than 10 mm/h and it does not impede the performance as the datasheet says. It is not specified how the performance of the radar will be affected by larger rainfall rates so there is no comparison for this.

Weather	Amount of measurements
Normal	3
Fog	5
Rain	8
Snow	2

Table 3.3: Categories of available in database measurements

Based upon their tags the measurements have been divided into different weather categories (see table 3.3).

One of the problems with the measured on the roof dataset is that the setup on the roof has not always remained the same throughout the long period of measurements. Some of the antennas have been moved or the radar might have moved, but what exactly happened

is unknown. This makes it difficult to draw definite conclusions over scans, especially separated by long time intervals. To clear some things up some new measurements have been done with the same radar with a different setup. This made it possible to verify the results with a few new measurements. To ensure this a cylindrical target has been placed in front of the radar and observed during a few intervals with and without precipitation.

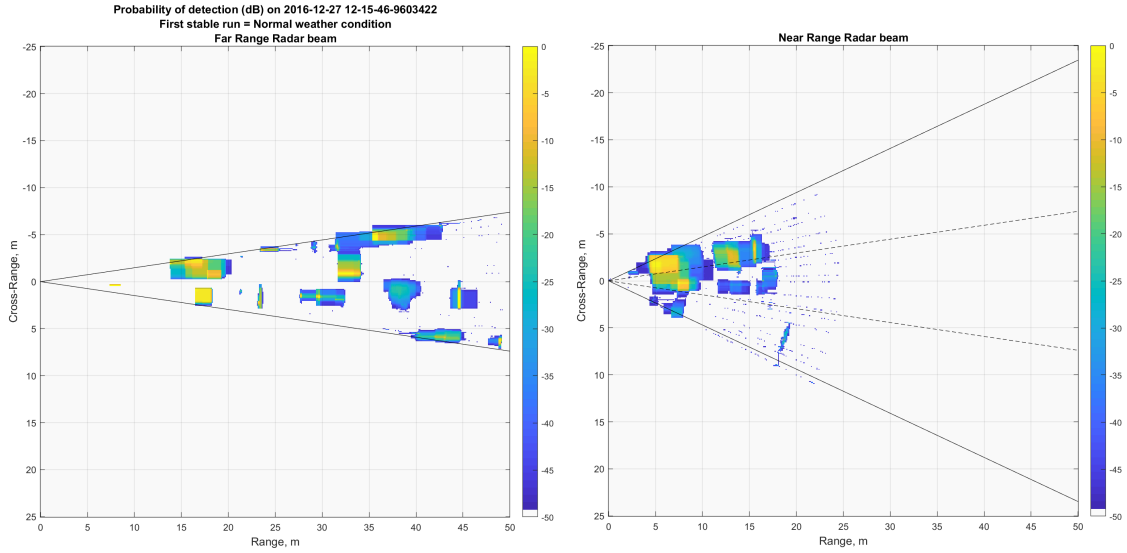

Figure 3.3: Probability of detection P_D of objects of opportunities on roof

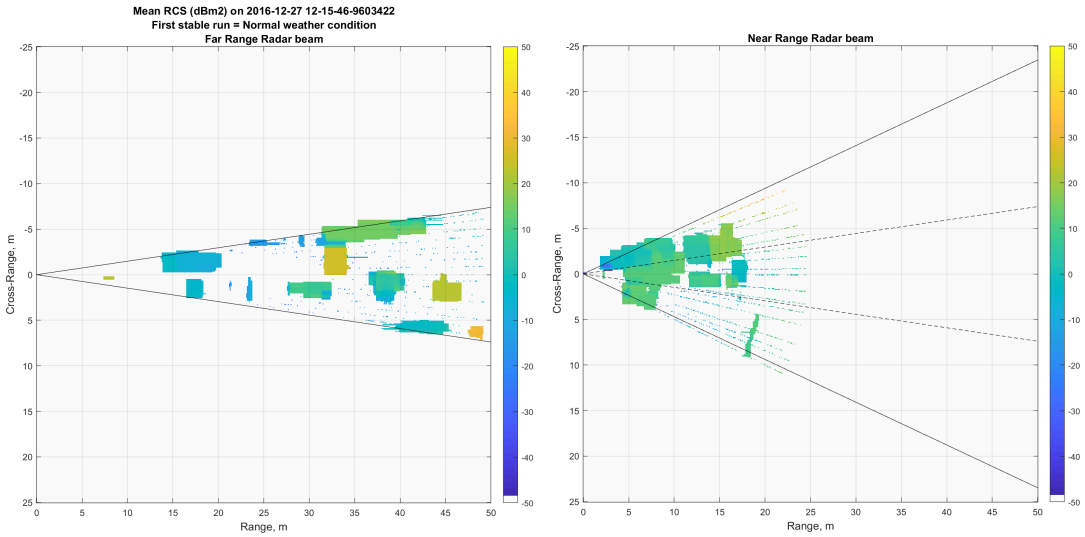

Figure 3.4: Mean RCS of objects of opportunities on roof

Figures 3.3 and 3.4 both show an example of what is seen by both of the beams in one of the available datasets. This dataset is one where the weather is normal and there are no weather factors that influence the measured target parameters. This illustrates what type of data is available.

Figure 3.3 takes all of the detected targets in all of the observed scans and plots where they are located on the 2D range-azimuth map. It also show with which probability these detections are seen at specific 2D resolution bins of this map. This might give some insight in which of these detections might be false alarms and where these occur.

It is unsure how exactly the radar defines a detected target. If an object is reported by the radar at the radar output interface as detected at a certain range and angle, in this thesis

we assume that the middle of the object is given and that the object stretches left and right to half of the reported length. Also that the object stretches towards its detection point plus the given width. There is no indication of this in the datasheet at all and this is just what was assumed based on radar basics and common sense.

In some cases there were no reported width and length associated with a detected target and in those cases there is only one 2D bin with the given range and angle was used to update the probability of detection. This shows how much variation there is for the detections and which targets remain fairly constant throughout the measurements.

It is interesting to note here that in this image there are straight forward narrow lines of detections appearing in the radar visions. These are most likely false detections, however why these false detections extend into these patterns is not clear from available for analysis information. It appears to happen in both of the radar beams, but is more visible in the near-field radar beam. Most likely that this effect has something to do with the resolution of the radar in azimuth that is lower for the near-field radar beam.

Figure 3.4 presents the mean RCS of all of the detections of all the targets in every 2D resolution bin. It shows the variability of spatial distribution of the RCS for every observed during specific measurement target. This might help with the targets associating in the sequence of scan and measurements, especially in cases when the situation on the roof has changed between the measurements.

3.3. Data association

The radar output includes a list of detections for every scan. In the detection mode, which was used for measurements with the radar on the roof of the EEMCS building, there is no data association between scans. This is what needs to be done to be able to create a model of the influence of precipitation and other different weather conditions on the observed characteristics of the cylindrical target (and perhaps other targets).

As soon as both the target and the radar are not moving, a Nearest Neighbour (NN) algorithm has been proposed to be used to cluster the data. Data association for a moving radar might require more advanced processing.

Detections are associated to the target by looking in a certain grid around the target. The grid is only specified in location (range and angle). There is no limitation for the target in any other parameters statistic (like RCS). This means that the possible false detections that have a wildly different RCS are not taken into account. As result, there might be some outliers of different target associated falsely in the measurement. To avoid this the period of spatial grid must not be taken too large. This located grid does not need to be updated between detections as the object that is studied is standing still.

When there are two possible detections, the one closest to the middle of the grid is chosen. The other one is thrown away so there is only one detection is taken into consideration on every cycle. The case of having multiple detections only happens in the near-field radar beam and this is most likely due to the size of the bins compared to the grid. It is however not the case that the detections are split into two 'half' detections. If in the other case no match is found in the grid it counts towards the not tracked percentage.

3.4. Discussion of results

After the data association the obtained results are visualised in the histograms in this section. The histograms that have been created show the course of the data over time. All measurements have been divided into N parts of 5 minutes duration. The images were created with 50% overlap to smooth them. All images show the near-field radar beam unless otherwise specified. If an object is not detected within the grid in a certain iteration the values will be collected in the rightmost bin of the image to allow every histogram to retain the same amount of iterations.

The metrics that will be compared are: the distance to the target, the azimuth angle to the target and the measured RCS of the target.

3.4.1. Comparison near- and far-field radar beam

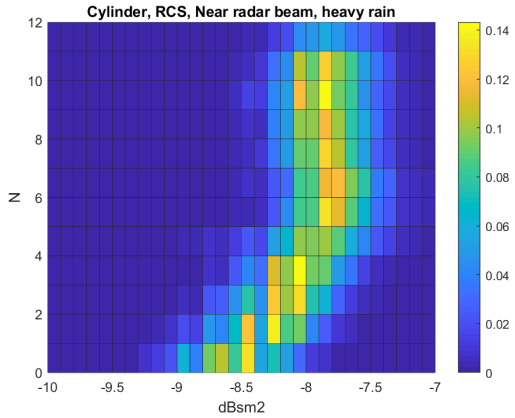

Figure 3.5: RCS of cylinder, near-field beam, heavy rain case

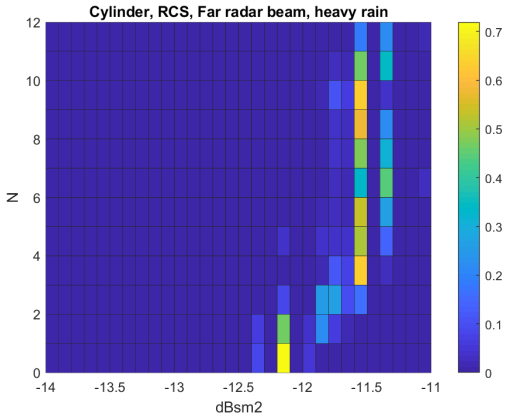

Figure 3.6: RCS of cylinder, far-field beam, heavy rain case

The targets are detected differently by the near- and far-field radar beams. To illustrate that these beams show the same variation, Figures 3.5 and 3.6 present the comparison of observations with them the same target. These images show the vertical cylindrical target that was observed in heavy weather conditions. To easily compare the two beams the same 2D grid size has been taken. It causes some issues with the far-field beam as there are some gaps in gridded data appearing due to the difference in resolution, but the equality in grids makes it easier to compare data from different beams. Two images show the same comparable shift in RCS at the same time of the measurement. As it was mentioned before, there is a difference between the two beams in mean observed RCS. In presented case it is equals to nearly 4 dBsm2 in mean RCS, but other cases show that it can vary depending on the type of target.

3.4.2. Weather analysis

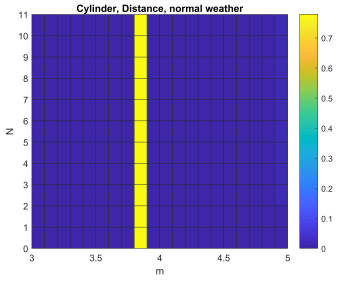

Figure 3.7: Distance to cylinder, normal weather

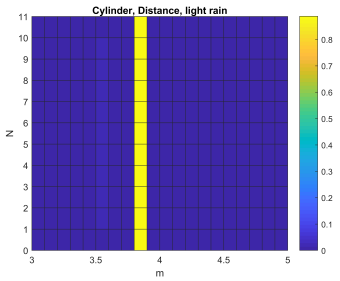

Figure 3.8: Distance to cylinder, light rain

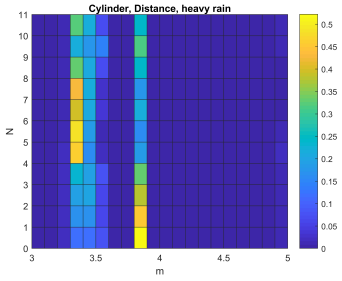

Figure 3.9: Distance to cylinder, heavy rain

The presented here images demonstrate the weather dependence of observed radar parameters for two different objects. Figures 3.7 until 3.15 shows the known vertical cylindrical target that was placed in front of the radar, while Figures 3.16 until 3.24 shows an object that has remained on the roof throughout the whole period of measurements. It is an extended object with a high RCS.

The cylindrical target is located at at distance of 3.8m and azimuth angle around -4.3 deg. Its RCS as seen by the near radar is around -8.5 dBsm2. The other target is an extended structure located at a distance of 14m and and angle around -10.5 deg with a much higher RCS of around 8 dBsm2.

Looking at these images it can be seen that the deviation in location is very small for all detections. The object is almost always detected at the same range, especially when the weather is normal. Only when it starts raining quite heavily a change in the distance to the

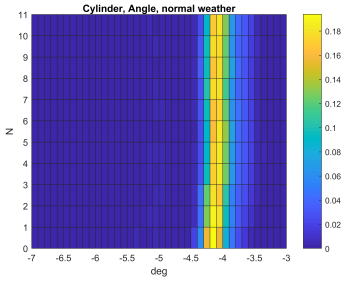

Figure 3.10: Azimuth angle to cylinder, normal weather

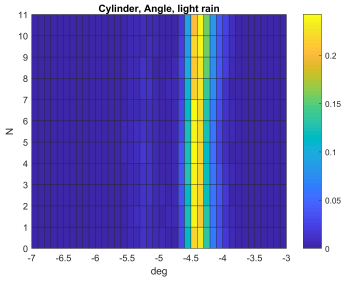

Figure 3.11: Azimuth angle to cylinder, light rain

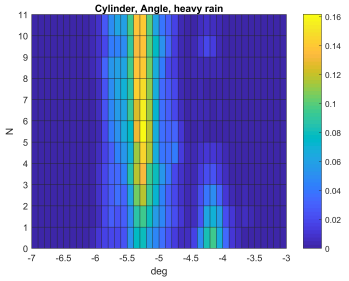

Figure 3.12: Azimuth angle to cylinder, heavy rain

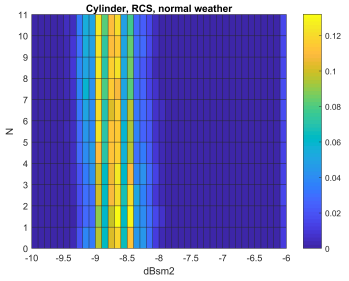

Figure 3.13: RCS of cylinder, normal weather

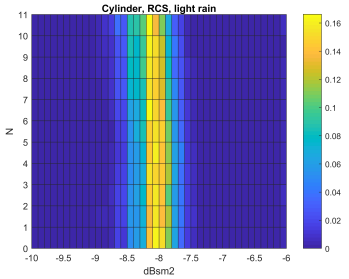

Figure 3.14: RCS of cylinder, light rain

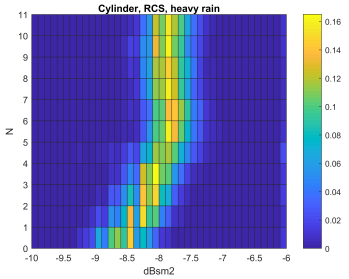

Figure 3.15: RCS of cylinder, heavy rain

target can be observed. For the cylindrical target the object is shifted by 0.3 - 0.5m during the rainy measurement.

For all characteristics there is a slightly larger spread of values when the weather is severe. This is not as visible in the distance as the changes here are small, but it is visible for all other variables.

The most interesting change can be see in Figures 3.15 - 3.24. These are both heavy rain cases and in both cases a shift in average RCS can be observed. During the measurement the average RCS of the object increases and the observed change is roughly the same for both objects. The change is most likely tied to the varying rainfall intensity.

In Figure 3.25 the average RCS of the cylindrical object is compared for all datasets. Here we see that within the heavy rain measurement the average RCS changes by 0.7 dBsm2 within the measurement. For the normal and light rain case the average RCS remains constant throughout the measurement.

The same trends can be seen in Figure 3.26 were a target with a high RCS was taken. The increase in RCS that can be seen here is larger: up to nearly 2 dBsm2 within the same measurement. This gives an indication that the size of the increase is related to the RCS of the target.

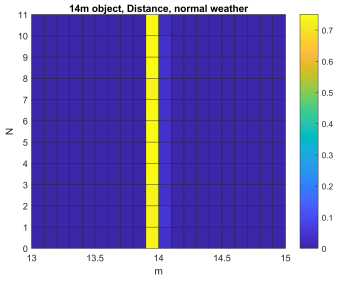

Figure 3.16: Distance to object, normal case

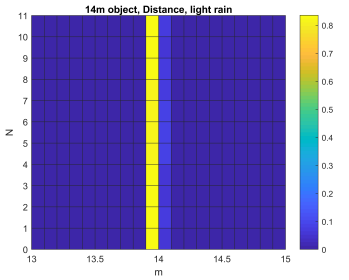

Figure 3.17: Distance to object, light rain

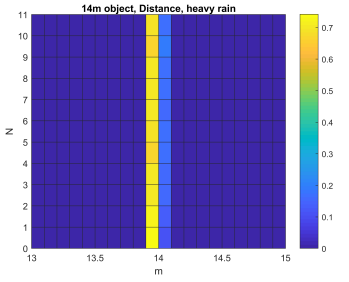

Figure 3.18: Distance to object, heavy rain

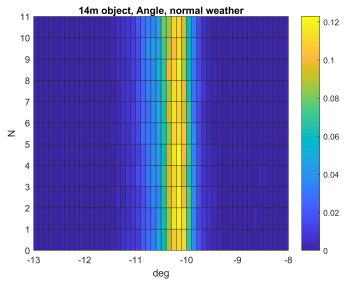

Figure 3.19: Azimuth angle to object, normal case

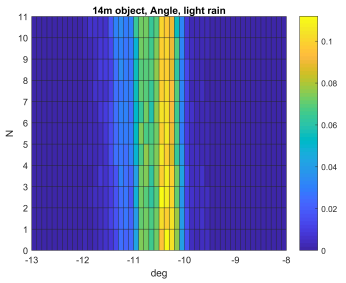

Figure 3.20: Azimuth angle to object, light rain

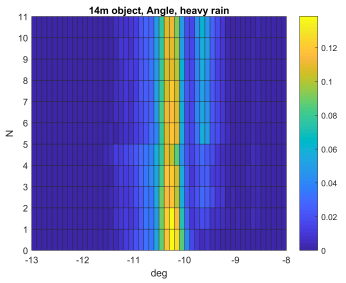

Figure 3.21: Azimuth angle to object, heavy rain

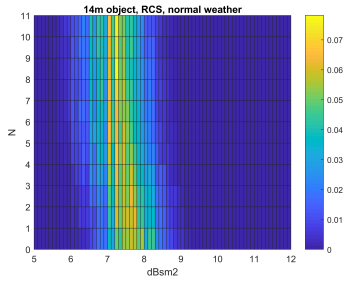

Figure 3.22: RCS of object, normal case

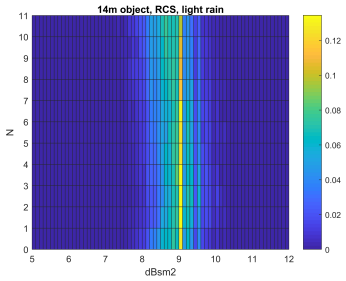

Figure 3.23: RCS of object, light rain

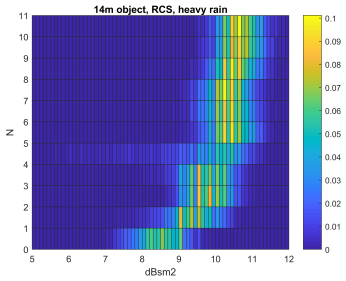

Figure 3.24: RCS of object, heavy rain

Another change between the different weather cases that can be detected, is that for the light rain case the average RCS is higher than for the dry weather case. This phenomenon is consistent over all objects. For the cylindrical target this difference is roughly 0.6 dBsm2.

For the higher RCS target this is an average RCS that is nearly 1.5 dBsm2 higher. The size of this increase does again seem to vary depending with the RCS of the target.

Cause for the RCS increase

What exactly causes these RCS increases? Usually there is an attenuation in RCS due to propagation through rain that is in the order of a few dB/km [34]. The objects that are detected on the roof are at most 30m away, so the effect of this should be very low.

What is seen in this data is however not an attenuation in RCS, but an increase. The increase appears during the measurement when it is raining heavily.

During rain the objects that are target become wet and this could cause the objects to be better visible to the radar because of the moisture layer on the target that creates a better reflective surface. Research [23] shows there should not be a change in RCS when comparing a wet and a dry reflector so this will most likely not the answer.

Looking further at the environment it must be noted that the floor of the roof is made of concrete. During heavy rain puddles are formed that might produce reflections that cause this. The radar backscatter increases when the concrete is wet and this could cause the increase in RCS due to stronger multi-path component of the received signal. This theory is supported by [13], [19] and [27] where measurements have been done that show that the backscatter coefficient increases during both different weather events and the state of underground.

The increase in RCS is linked to the rainfall rate as it changes throughout the measurement. It might also be that it is linked to the wetness of the concrete surface and that prolonged rain would have the same effect as one heavy rainfall.

3.5. Conclusion

There was a lot of data that needed to be analysed to take a look at what the influence of adverse weather conditions might be on the radar data. According to the datasheet the commercial radar should not be impaired in functionality during light rain, but nothing was

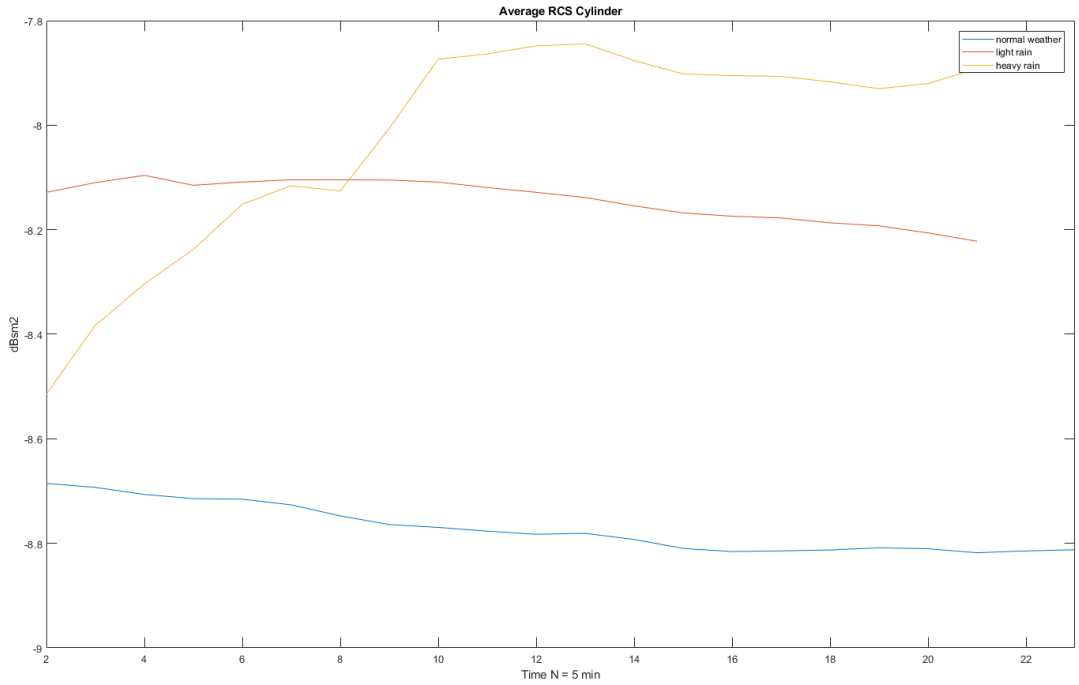

Figure 3.25: Average RCS for the cylinder against the iteration time

said for larger rainfall rates. The radar had two different radar beams that showed the same trends for objects, but were not easily compared because there was always a shift in where the target was detected. The data that was gathered had very loose weather labels attached to the measurement. The measurement that were gathered were of targets in stationary conditions and therefore a nearest neighbour algorithm was used to cluster the data and analyse it.

During a rainy event the radar appears to have almost no variation in how the target is detected in range, a little shift might occur in angle and a large shift in RCS. The data shows a shift in average RCS of an increase 0.7 dBsm2 within one heavy rain measurement. This shift is probably caused because of reflections of the wet concrete floor which increases the backscatter of the radar and thus the RCS of the target, as a result of multi-path propagation.

The variation of the target RCS is slow and thus can be neglected when observing targets in the operational mode.

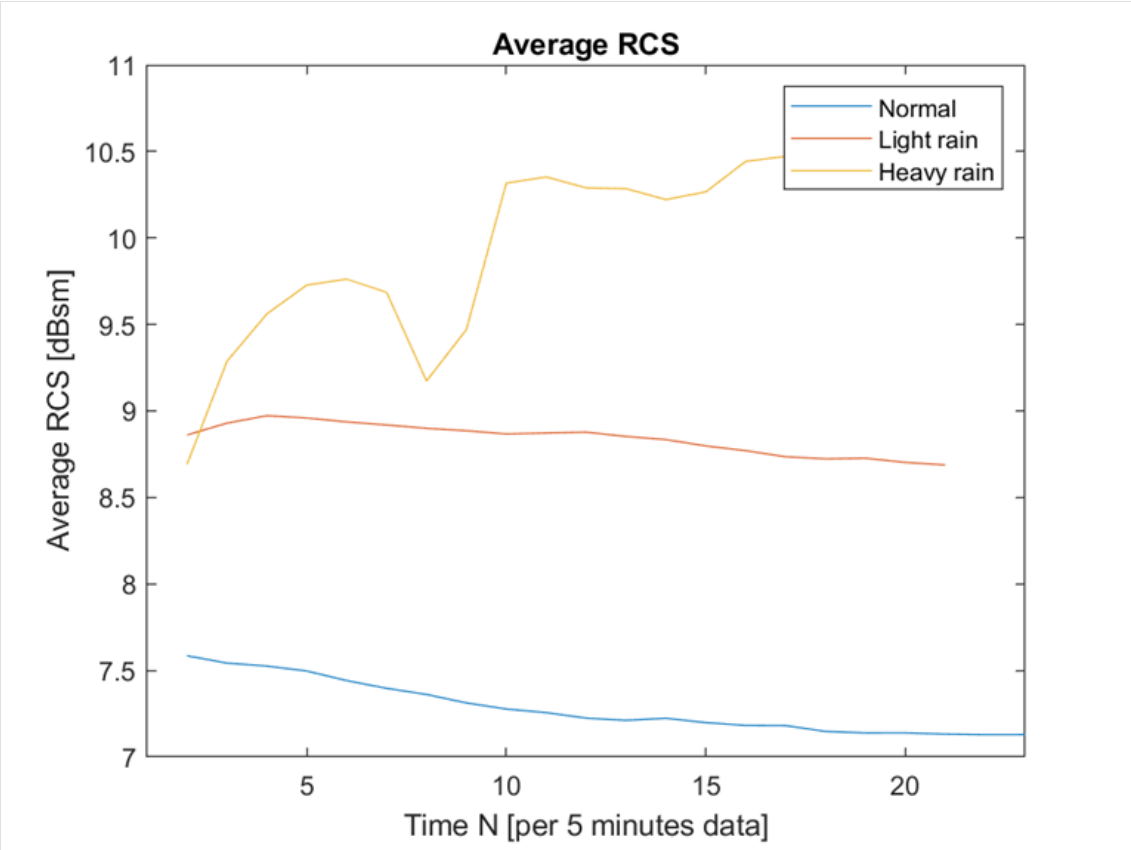

Figure 3.26: Average RCS for high RCS target

4

Estimating of calibration coefficients

In this chapter, the techniques for antenna array calibration in presence and absence of mutual coupling will be investigated.

These algorithms are analysed in terms of the number of required observation and the angular sector over which the targets are observed. Application of a moving platform with sequential estimation of the targets at different range or angular location is also considered.

The distortion that needs to be estimated consists of both a linear amplitude and phase component that is different for each element. It is described in the complex coupling matrix $\boldsymbol{C}$ which describes the coupling coefficients for each antenna element. The estimation tries to find the elements of the calibration matrix T which should in theory perfectly cancel out the negative effects of the coupling matrix.

It is important to properly calibrate the array as [2] shows that "coupling causes an error in the detected angle of the target by as much as 12 deg and an increase in the beamformed response sidelobe level of as much as 8 dB."

4.1. Estimation algorithm with mutual coupling

This section will expand further on the algorithm [28] on which the two approaches are based. The example has M antenna elements and P measurements. The estimation algorithm needs P measurements of targets, but not of P targets. Calibration with a moving radar makes it possible to use multiple measurements of the same target that has moved in the radar's field of view. This is likely to happen in the scenario where objects of opportunity are measured.

There are two approaches to estimate these calibration coefficients. In the first approach the full calibration matrix is estimated, which includes not only amplitude and phase distortion of every antenna element, but also the coupling coefficient between each couple of elements.

The second approach estimates only amplitude and phase distortion of every element. This is a simplification as the calibration matrix is a full matrix, but this improves the speed and stability of the algorithm.

Both approaches require the angular position of the targets to be known beforehand. This need to know the locations of the targets limits applicability of these algorithms to radar calibration in the operational mode.

Both of the approaches work with the same principle. The calibration matrix $\boldsymbol{T}$ can be defined as the matrix that shows the difference between the ideal signal matrix $\boldsymbol{S}$ and the measurement matrix $\boldsymbol{X}$ that has been distorted.

$$\boldsymbol{TX} = \boldsymbol{S} \tag{4.1}$$

The locations of the targets need to be known for this method as they will be used to construct the ideal signal matrix $\boldsymbol{S}$. The mathematical model that is used to construct this

matrix can be described as this:

$$\boldsymbol{S} = [\boldsymbol{s}_1 \boldsymbol{s}_2 \dots \boldsymbol{s}_M] \tag{4.2}$$

where every column gives the contribution of one antenna element.

The measurements are gathered in the matrix $\boldsymbol{X}$ which consists of P measurements with targets at a known angular position $\theta_{t,p}$. It is assumed that the angle and the configuration of the radar array is known beforehand; the range r to the target can remain unknown. These angles are used to create the ideal signal model that will be used in the algorithm.

The measurement matrix $\boldsymbol{X}$ is corrupted by the coupling matrix $\boldsymbol{C}$ and noise $\boldsymbol{N}$:

$$\boldsymbol{X} = \boldsymbol{CS} + \boldsymbol{N} \tag{4.3}$$

It consists of P measurements of targets:

$$\boldsymbol{X} = [\boldsymbol{x}_1 \boldsymbol{x}_2 \dots \boldsymbol{x}_P] \tag{4.4}$$

The calibration matrix T can be found with the least squares estimator as:

$$\boldsymbol{T} = \underset{\boldsymbol{T}}{\operatorname{argmin}} ||\boldsymbol{S} - \boldsymbol{TX}||_F \tag{4.5}$$

$$\boldsymbol{T} = \boldsymbol{SX^H}(\boldsymbol{XX^H})^{-1} \tag{4.6}$$

The algorithm uses the least squares approach to estimate the calibration matrix $\boldsymbol{T}$. In order to have matrix $(\boldsymbol{XX}^H)$ invertible, the matrix $\boldsymbol{X}$ should consist of $P > M$ independent measurements at different angles [28]. This ensures that the matrix $\boldsymbol{XX}^H$ is of full rank and thus will be invertible.

As mentioned earlier the angles $\theta_{t,p}$ of the targets need to be known. From these angles the ideal signal model can be created and they will be based on the relative signal phases ϕ between the antenna elements. They can be calculated in this way:

$$\phi(m, \theta_{t,p}) = 2\pi \frac{c_0}{f_0} y_{RX}(m) sin(\theta_{t,p}) \tag{4.7}$$

where c_0 represents the speed of light, f_0 the operating sweep start frequency and y_{RX} the positions of the antenna elements.

The ideal signal model $\boldsymbol{S}$ can then be calculated by relating the relative signal phases to the signals measured at the first element $m = 1$. These removes the absolute phase component and leaves only the relative amplitude and phase relations between the elements.

If the first element is used as a reference, we get the ideal signal model:

$$s = x(r, 1)[1 e^{j\phi(2,\theta_{t,p})} \dots e^{j\phi(M,\theta_{t,p})}]^T \tag{4.8}$$

In presence of amplitude instabilities between the elements the performance of this algorithm depends a lot on the magnitude of the calibration coefficient of the first element. This method gives an (in theory) perfect estimation when the distortion consists of only phase errors. It does not however give a good estimation for when there are also amplitude errors occurring.

When the first element is a largely distorted channel compared to the other elements, the algorithm does not give a good estimate. However there are M options for channels that can be chosen as a reference. One way to address this problem is to perform pre-processing to decide which channel would be best as a reference channel. A similar approach has been studied in [14].

In Figures 4.1 and 4.2 every of the antenna elements have been taken as a reference element. This shows that there is a best option for the reference element and that there can be a rather large gap in performance depending on which reference element is chosen.

The question now is what kind of metric will give a good estimate to determine which channel to use. This will all depend on the type of amplitude error that is degrading the performance of the array. For now there are two types of amplitude errors that are considered:

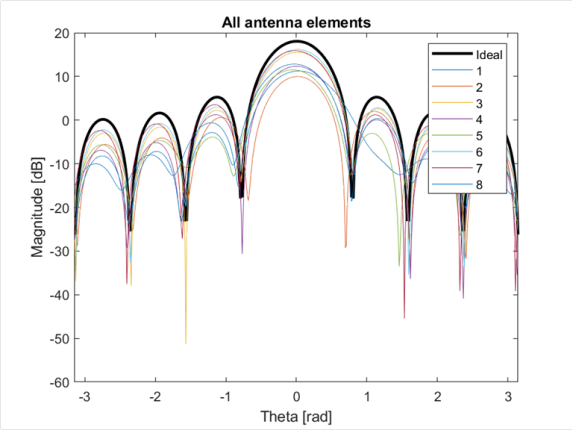

Figure 4.1: All possible reference elements with degrading error

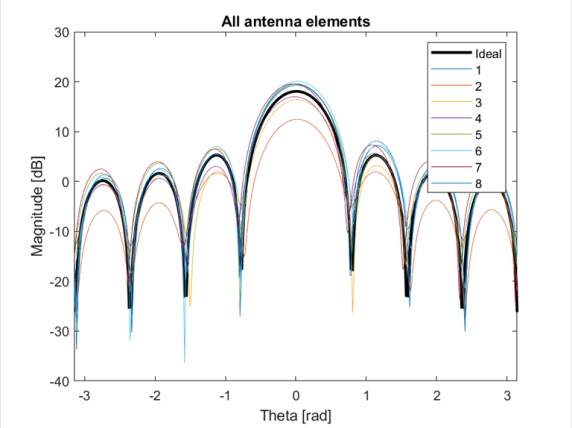

Figure 4.2: All possible reference elements with centred error

either the amplitude is always degrading or amplitude is centred around the true value. These are also the options shown in Figure 4.1 and 4.2.

If the amplitude is always degrading it means that every element $|C_{ij}| < 1$. In this case the best channel will be the one that has the maximum mean power of all of them as this will be the one where the power is closest to the 'true' value of the amplitude.

To show how the estimation recreates the beam pattern Figure 4.3 and 4.4 show 100 realisations of the recreated antenna pattern. These antenna patterns have been normalised to their maximum value to be able to compare them. The degradation in this case was chosen to be normally distributed $C_{ij} \sim \mathcal{N}(0.6, 0.1)$ so that all values are degrading.

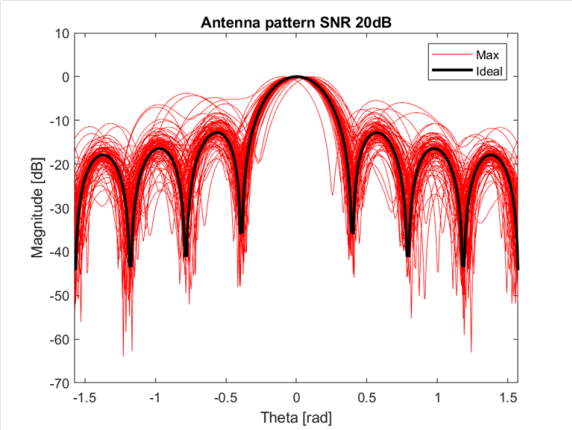

Figure 4.3: Antenna pattern with degrading error at SNR 20 dB

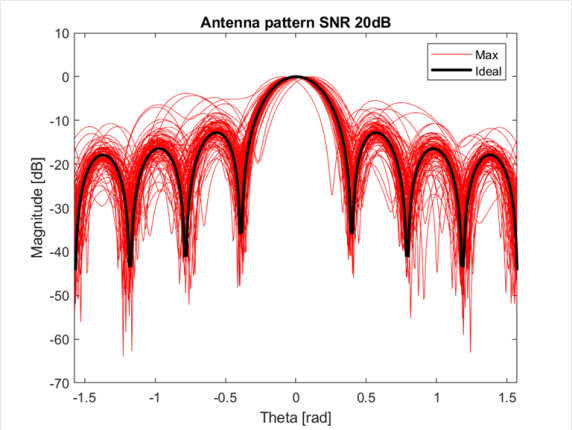

Figure 4.4: Antenna pattern with degrading error at SNR 30 dB

When the amplitude is centred around the true value the best option will either be the channel closest to the mean or median of the channel. In this case the values C_{ij} are chosen to be centred around 1 so that $C \in \mathcal{U}[0.5, 1.5]$.

Both of these metrics actually perform comparably; it depends on the individual case which one of these will give the better results. These can be found in Figures 4.5 until 4.8.

It will be difficult to predict what type of error will actually be encountered in real measurements as usually not a lot is known about the production error.

Factors influencing the estimation

There are several factors that influence the quality of the estimation: SNR, M number of antenna elements, P the number of measurements used and the accuracy of the target's angular locations.

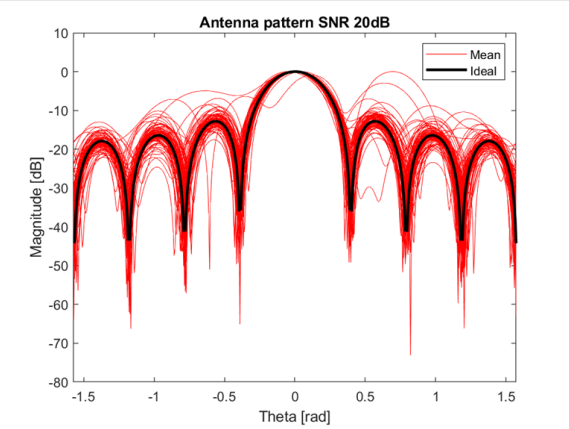

Figure 4.5: Antenna pattern with centred error and mean estimator at SNR 20 dB

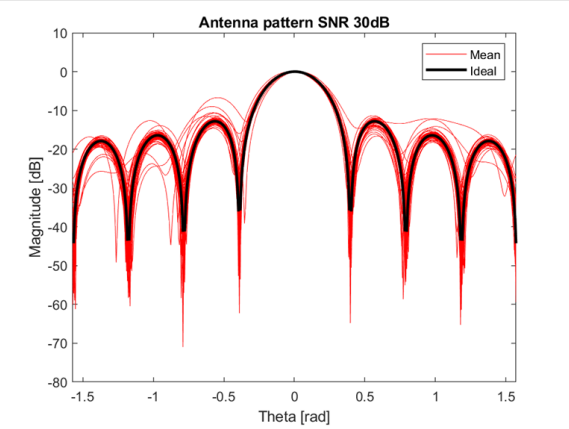

Figure 4.6: Antenna pattern with centred error and mean estimator at SNR 30 dB

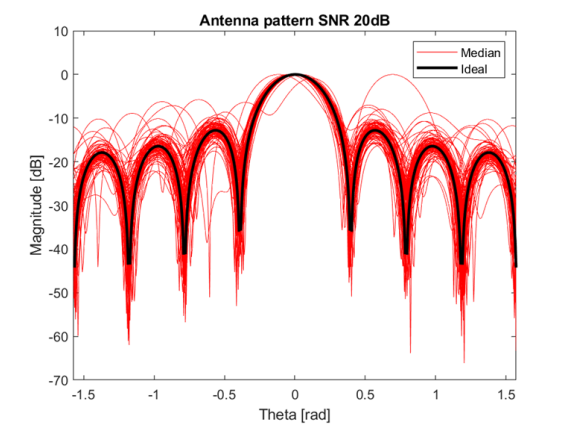

Figure 4.7: Antenna pattern with centred error and median estimator at SNR 20 dB

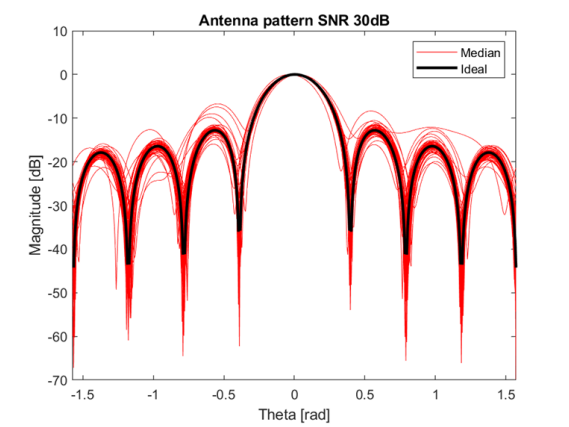

Figure 4.8: Antenna pattern with centred error and median estimator at SNR 30 dB

The impact of target SNR on the estimation performance can be seen in the images above. With higher SNR the antenna pattern will always be closer to the ideal antenna pattern and there is not much variation between them. The SNR at which a target is picked up and used for the estimation should not be lower than 15 dB. There will be distortions in the antenna pattern below this threshold.

Another factor that has an effect is how close the targets are located over the observed angles. The effect of this is very small, only when they are exactly the same the estimation will diverge. The target location has larger impact when the SNR of target is low. However when the SNR $\geq$ 15 dB this will not pose a problem.

The performance of the estimation depends on the relative number of measurements (P/M), which implies that calibration of a larger array will require more measurements to converge.

When the number of antenna elements M is higher the number of elements that need to be estimated is also higher and this negatively affects the estimation. That means that when the number of antenna elements is higher that the estimation will be worse if none of the other factors are changed.

For the fixed antenna size, the number of measurements plays a crucial role. The algorithm requires $P > M$. The accuracy of the estimation improves with increasing P. This is an easy way to increase the quality as it is possible to keep on growing the list of measurements that are used as the radar encounters more targets.

The estimation algorithm needs to know the angles beforehand to be able to construct the ideal signal model. Figure 4.9 and 4.10 show however that it can operate well with a

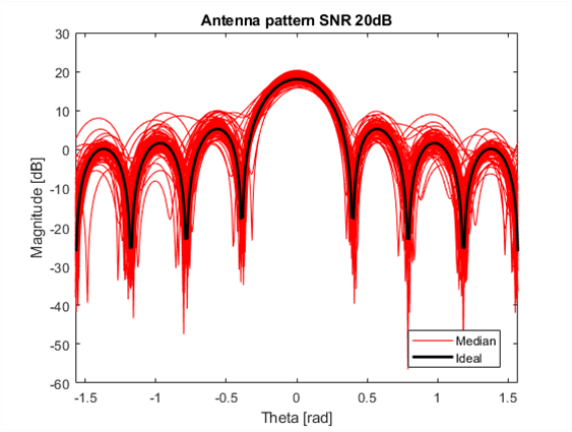

Figure 4.9: Antenna pattern with accurate angle

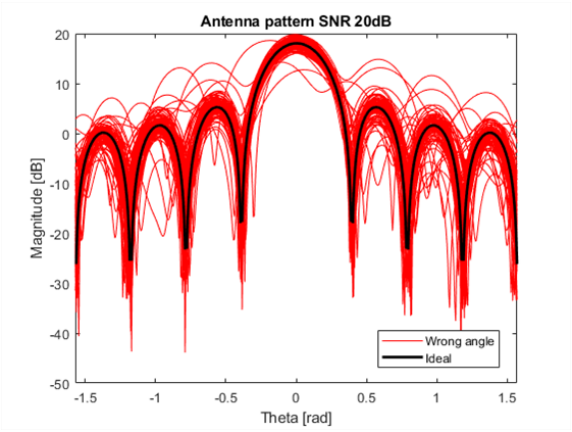

Figure 4.10: Antenna pattern with inaccurate angle

moderate angular errors. In Figure 4.10 the angle is distorted by $\sim \mathcal{N}(0°, 10°)$. This is quite a large distortion and the distortion of the antenna pattern is not that noticeably larger than before. This shows that accurate target positioning plays a role in the estimation accuracy, hence this is not detrimental for the overall calibration performance.

To sum up, calibration with the coupling is sensitive to the number of observed target, has moderate stability with respect to angular locations of the targets and requires targets an $SNR > 15dB$ and the number of measurements $P > M$ to perform reliable calibration.

4.2. Estimation algorithm without mutual coupling

If no mutual coupling is present, the calibration matrix in equation 4.1 is a diagonal matrix and the estimation procedure can be simplified. Negligible mutual coupling is often assumed for MIMO arrays due to large spacing between transmitted antennas [4]. This method works when this is the case and it allows us to divide the problem in smaller parts and calculate every coefficient separately. In this way the estimation does no longer need full matrices that need to be inverted. This is a good improvement as this creates a stable solution with less measurements.

Recall from equation 4.1 the relation between measured signals and ideal signals. Now if the matrix $\boldsymbol{T}$ consists of only a diagonal matrix it can be written as:

$$\begin{bmatrix} t_1 & 0 \\ 0 & t_2 \end{bmatrix} \begin{bmatrix} x_{11} & x_{12} & x_{13} \\ x_{21} & x_{22} & x_{23} \end{bmatrix} = \begin{bmatrix} s_{11} & s_{12} & s_{13} \\ s_{21} & s_{22} & s_{23} \end{bmatrix} \tag{4.9}$$

Here there are two antenna elements in T and no mutual coupling terms between them. There are three measurements in the matrix. These equations can be taken out of the matrix because there is no mutual coupling. Taking a look at the equation for the i-th calibration coefficient gives:

$$t_i \begin{bmatrix} x_{i1} & x_{i2} & \dots & x_{ij} \end{bmatrix} = \begin{bmatrix} s_{i1} & s_{i2} & \dots & s_{ij} \end{bmatrix} \tag{4.10}$$

$$t_i \boldsymbol{x_i} = \boldsymbol{s_i} \tag{4.11}$$

Solving 4.12 for t_i gives:

$$t_i = \frac{\boldsymbol{s_i x_i}^H}{\boldsymbol{x_i x_i}^H} \tag{4.12}$$

By doing this it is possible to calculate all of the calibration coefficients separately. Compared to the estimation 4.1, this requires to estimate only M unknown coefficients compared to M^2 of 4.1, which makes this solution more stable in presence of limited number of observations. This calibration can work with as few observations as one.

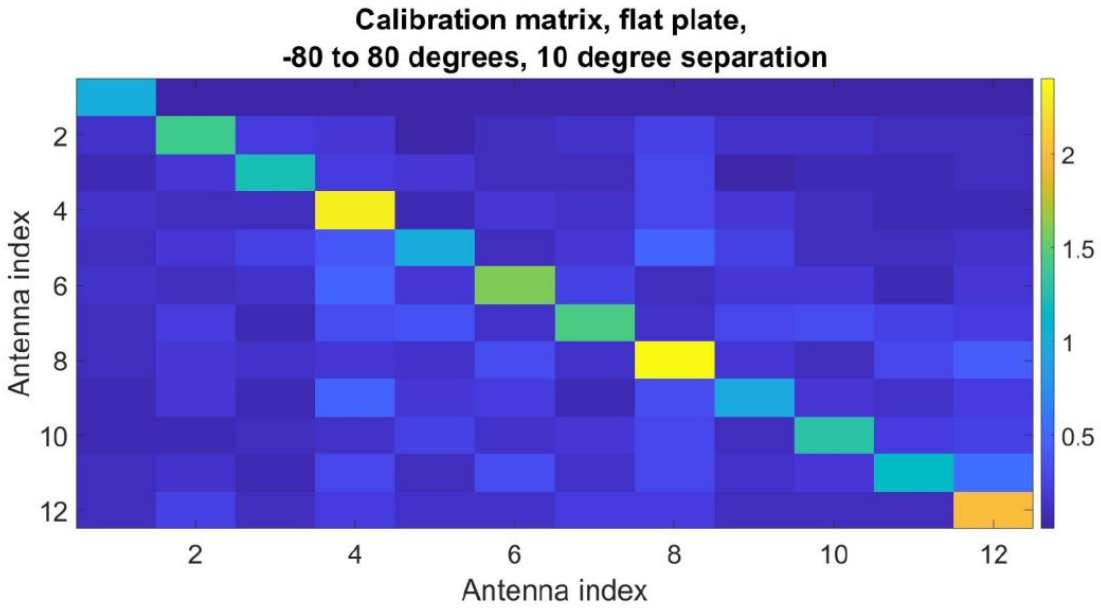

Figure 4.11: Calibration matrix as calculated by measurement with a MIMO radar. Figure taken from [5]

The large disadvantage this method has is that it is not able to work with mutual coupling factors between the antenna elements. As MIMO radar often uses a virtual array that is much larger than the actual amount of available arrays the effect of the mutual coupling is not that severe. This effect can be seen in Figure 4.11. In these figures the calibration matrix for a MIMO radar is represented and the largest contributions to this matrix are on the main diagonal. Therefore the method without mutual coupling might be sufficient for the application, especially when enough steps are taken to shield the antennas as much as possible [14].

4.3. Moving radar

The estimation algorithms needs P measurements of targets, but not of P targets. This makes it possible to use multiple measurements of the same target that has moved in the radar's field of vision as is described in Figure 4.12.

The reflection of the target will remain roughly the same but the SNR increases when the target approaches. The SNR increases by a power R^4 as is described by the radar range equation.

Looking at the radar range equation in [30] it relates the relationship between the transmitted and received signal power, gain of both the transmit and receive antennas,

$$P_r = \frac{P_t \lambda^2 G^2 \sigma}{(4\pi)^3 R^4} \tag{4.13}$$

The radar system is known beforehand and can be viewed as a constant C_0^2 in this derivation. Doing this the radar equation tells us that the received signal can be calculated if the distance to the target R, the angle θ at which the target is located and the radar cross section σ of the target is known.

$$P_r = C_0^2 f(\theta, R)\sigma \tag{4.14}$$

where the radar cross section $\sigma = |\alpha|^2$

The function $f(\theta, R)$ consists of the range R to the target which decrease the received signal by a power of four and the θ comes into this factor by the gain G. In this case both the transmit and receive antennas are equivalent so this factor can be represented as $G = cos(\theta)$.

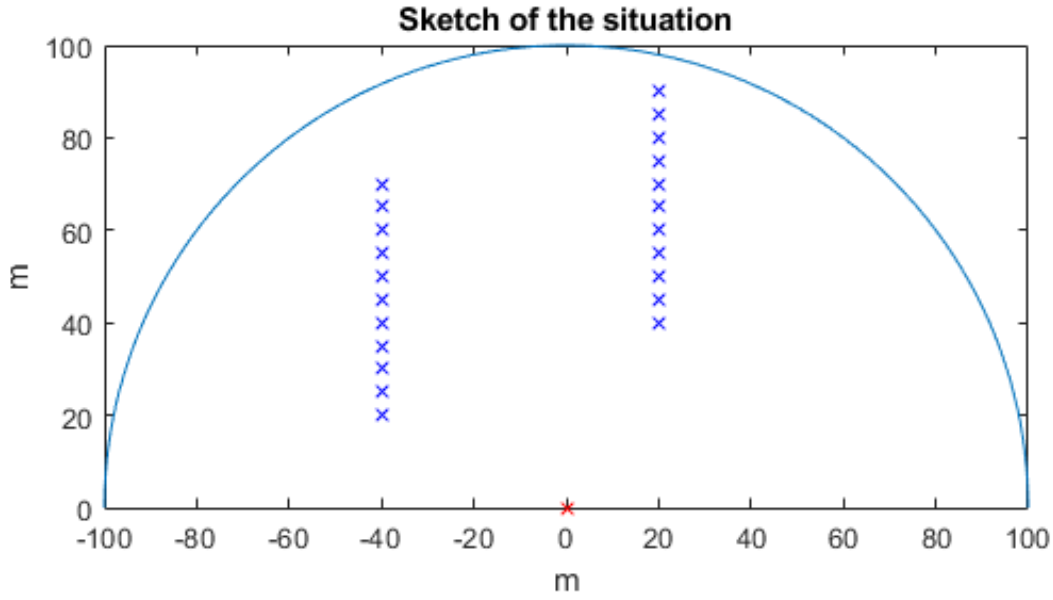

Figure 4.12: Sketch of the situation with two targets

$$f(\theta, R) = \frac{cos^2(\theta)}{R^4} = \frac{G^2(\theta)}{R^4} \tag{4.15}$$

If target has constant RCS (Swerling 0), its SNR increase will only depend on the distance between two measurements. Using this distance the new SNR can be calculated.

$$SNR = \frac{P_s}{P_n} = \frac{\lambda^2 G^2 \sigma}{(4\pi)^3 R^4} \sim \frac{1}{R^4} \tag{4.16}$$

As the range will decrease as a target is moving closer within the range of the radar the SNR of the target will increase. A higher SNR target will produce a better calibration estimation.

4.4. Conclusion

In this chapter two algorithms for collocated MIMO antenna array have been analysed. The algorithms uses real measurement data, but requires the angles of the measured targets to be known beforehand. From these angles an ideal signal model can be created and used to solve for the calibration coefficients in a least squares sense. The angles should be known within a few degrees to provide reliable calibration.

The two algorithms are based on the same principle, but the difference between them is that first one tries to estimate the full calibration matrix with all of its mutual coupling coefficients and the second one estimates only the diagonal of the calibration matrix. Using just the diagonal appears to still give a good estimation and it adds stability to the estimation and requires less observations to obtain a stable solution. It allows us to separate the problem and look at each antenna element individually. This property will be used to track these variables in a Kalman filter in one of the following chapters.

5

Phase error distribution

In this chapter the relation between calibration error and beam-pointing error is investigated. First the normal and complex normal distribution will be defined and then the dependency of beam-pointing error of linear phased array on the calibration error is studied. The analysis evaluates for which calibration errors, the approximation [6] is valid and related this to the distortion of the main beam.

5.1. Complex normal distribution

The measurements are always the subject of noise. In most cases the noise that will be added can be described by the normal distribution [17]. A random variable x with mean μ_x and variance σ_x^2 is normal distributed when the pdf is given by:

$$p(x) = \frac{1}{\sqrt{2\pi\sigma_x^2}} exp[-\frac{1}{2\sigma_x^2}(x-\mu_x)^2] \tag{5.1}$$

This can also be written $x \sim \mathcal{N}(0, \sigma_x^2)$

Radar signal processing is often performed with the complex signal representation. The complex random variable $\tilde{x}$ consists of a real u and imaginary part v that are assumed to be independent of each other: $\tilde{x} = u + jv$. The standard definition also assumes that the real and imaginary parts both are Gaussian distributed so that:

$$u \sim \mathcal{N}(\mu_u, \sigma_u^2/2) \quad v \sim \mathcal{N}(\mu_v, \sigma_v^2/2) \tag{5.2}$$

For the definition of the Complex Gaussian distribution it is assumed that the parts have the same variance, but not the same mean. The joint distribution of these variables and thus the complex Gaussian pdf can be described as follows:

$$p(u,v) = \frac{1}{\pi\sigma^2} exp\left[-\frac{1}{\sigma^2}((u-\mu_u)^2 + (v-\mu_v)^2)\right] \tag{5.3}$$

This can be simplified by writing $\tilde{\mu} = E(\tilde{x}) = \mu_u + j\mu_v$. The complex Gaussian pdf can then be simplified in this way:

$$p(\tilde{x}) = \frac{1}{\pi\sigma^2} exp[-\frac{1}{\sigma^2}|\tilde{x} - \tilde{\mu}|^2] \tag{5.4}$$

5.2. Phase error distribution

These transformation will be useful for the stability of the algorithm in the next chapter. In total there are two transformations which are used to achieve this:

$$\sigma_{R/I}^2 \longrightarrow \sigma_{\psi}^2 \longrightarrow \sigma_{\hat{\phi}}^2 \tag{5.5}$$

Instead of describing the complex random variable $\tilde{x}$ through its real and imaginary parts it can also be described through its magnitude and phase components $\tilde{x} = u + jv = Re^{j\psi}$. First, we need relate the variance of the real part σ_u^2 to the variance of its phase equivalent σ_ψ^2. According to [33], for high SNR the pdf of the phase can be described as:

$$W(\theta) = \frac{a}{\sqrt{2\pi}} e^{-\frac{1}{2}a^2\theta^2} \tag{5.6}$$

This is a Gaussian distribution and a is defined as:

$$a = \frac{A}{\sigma_R} \tag{5.7}$$

Here A is the term for the SNR of the target while σ_R represents the standard deviation of the real part of the random variable.

Turns out that there is actually a linear relation between the phase part and the real part in terms of variance.

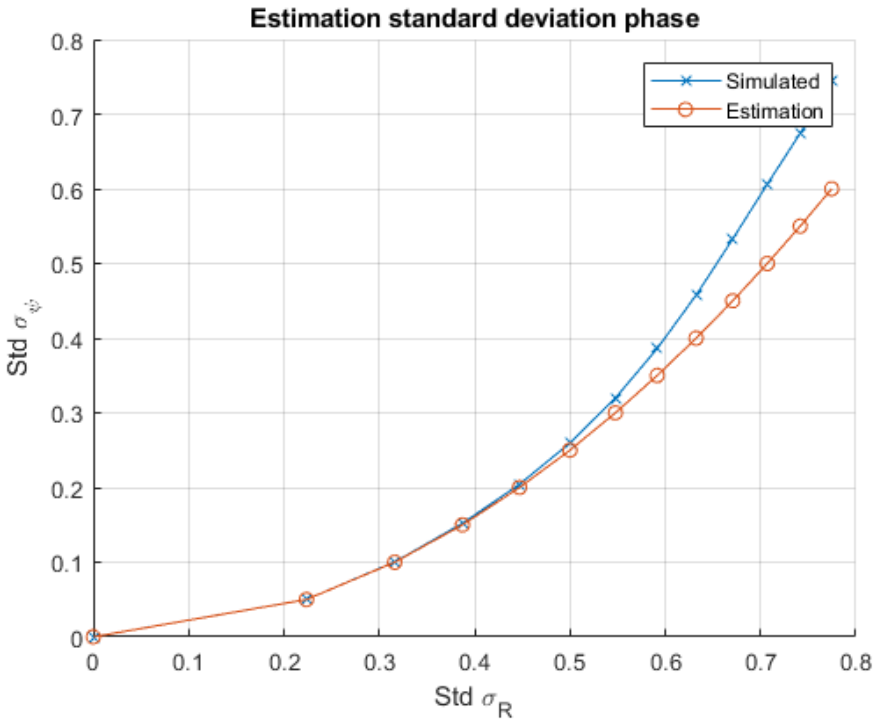

Figure 5.1: Estimation compared to simulated standard deviation

How well this estimation performs can be found in Figure 5.1 and 5.2, where it is assumed that A=1 (the average calibration coefficient on each antenna element). The estimation works near perfect for the low variances and starts to diverge for when the variance is over 0.4. This is the variance of one part of the random variable.

5.3. Beam-pointing error analysis

The paper [6] relates the beam pointing error to the phase distribution that was acquired above. The beam pointing error is the error that describes the error induces to target angle estimation by non-perfect array calibration. It has been shown in [6] that amplitude errors for the first order do not affect the beam pointing accuracy.

It also assumes that the beam-pointing error is just a small fraction of the beamwidth. The beamwidth of a MIMO system with $M = 8$ elements has a beamwidth of roughly $0.89 * 2/M$

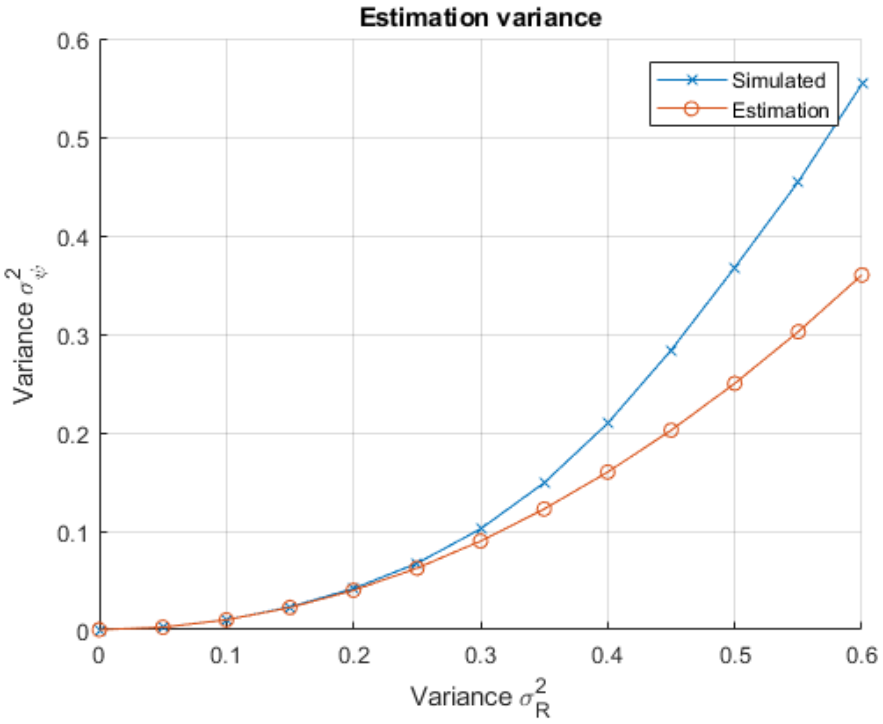

Figure 5.2: Estimation of variance compared to simulated variance

which is approximately 0.22 for the full beam and half of that 0.11 to compare it to the shift in angle.

The beampointing error is related to the phase error by the following expression:

$$\Delta\theta_{rms} = \frac{23^{1/2}\sigma_\psi}{kdcos\theta_0 F^{1/2}} \tag{5.8}$$

Here $k = 2\pi/\lambda$ stands for the wavenumber, d the distance between the antenna elements and θ_0 the direction in which the beam is pointed. For a linear array:

$$F = (M-1)M(M+1) \tag{5.9}$$

and F can be approximated to $M^{3/2}$ for a large array. It can be seen that approximation already holds for $M = 8$ elements:

$$\frac{\sqrt{((M-1)M(M+1))}}{M^{3/2}} = 0.9922 \tag{5.10}$$

In theory there should be a difference of less than 1% between this approximation and the real elements, even for only 8 antenna elements. This will be more accurate for an array with more elements.

Taking this approximation and assuming that the phase errors are normally distributed with a small variance, gives the general equation to one for a linear array:

$$\Delta\theta_{rms} = \frac{2(3)^{1/2}\sigma_\psi}{kdcos\theta_0(M-1)^{3/2}} \tag{5.11}$$

The application of this linear relation 5.3 needs two questions to be addressed:

- How accurate this approximation is
- Up to which phase (or complex magnitude) error it is applicable

These questions are investigated through numerical simulations.

Numerical simulations

To be able to compare this approximation to simulated values it is necessary to find how large the shift is that is introduced when there are phase errors in the calibration coefficients. This shift can be found by finding the peak of the ideal antenna pattern and comparing it to the peak of the distorted pattern. To avoid discretisation of the beam-pointing error by the angular sampling, this shift is found using interpolation.

It is possible to find the maximum of the function by taking its largest sample and the two adjacent ones and interpolating the space between the grid point with a parabola. This is a lot less computationally expensive than taking a large Fourier transform and will usually produce an estimation with a better resolution that can usually only be achieved by taking a larger Fourier transform.

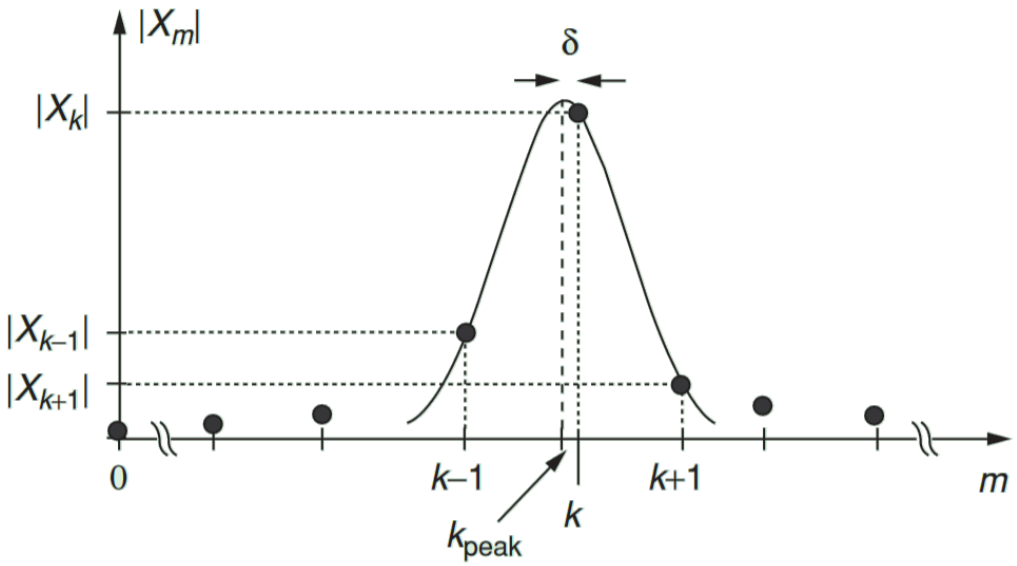

Figure 5.3: Interpolation of DFT variables; Figure from [16]

This technique uses only three samples: X_k, X_{k-1} and X_{k+1}: peak sample and the adjacent ones (the technique also works with some oversampling involved).

The paper in [16] proposes several solutions, but the expression that was chosen has no statistical bias and a good accuracy when the data is unwindowed. The expressions uses the complex DFT values rather than the magnitude as follows:

$$\delta = -Re\left[\frac{X_{k+1} - X_{k-1}}{2X_k - X_{k-1} - X_{k+1}}\right] \tag{5.12}$$

5.4. Combined analytical expression

Combining equations 5.2 and 5.3 gives us an expression that links the variance of the real and imaginary part to the variance of the phase error:

$$\sigma_\phi^2 = \frac{2(3)^{1/2}\sigma_R^2}{kd\cos\theta_0(M-1)^{3/2}} \tag{5.13}$$

In Figure 5.4 it can be seen that the estimation of the variance from [6] for just 8 antenna elements has a similar shape to the simulated variance. However the estimation varies more than the 1% that was predicted by the paper that describes the estimation.

The estimation works fine up to a point, but it diverges quickly for larger variances. This would mean that the estimation is valid for standard deviation of the real part of $\sigma_R \leq 0.7$;

which is equal to a variance $\sigma_R^2 \leq 0.5$. It implies that equation 5.4 can be used to predict the beam-pointing error only when $\sigma_R < 0.7$.

When the variance is larger than the cut off point this will show in a distortion of the main lobe and its location. This needs to be avoided and that is why it is important to stay in the operating region where the estimation overlaps with the simulated variance. It would be safe to assume that after the initial calibration in the garage that the radar should be in the operating region on the left of the cutoff point where there is no distortion in the main beam. The radar can then continue on from this point and start calibrating from the current estimation.

Larger number of antenna elements

Now going back the paper [6] mentions that the equation is only valid for small variances. The equation is not as accurate as was predicted, only for very small variances the estimation is identical to the simulated value. It diverges quickly away from the estimation.

The estimation was made for larger antenna patterns. Comparing Figure 5.5 where 64 antenna elements were simulated to Figure 5.4 where only 8 antenna elements were simulated it can be seen that the estimation performs better and stays valid longer for a larger amount of antenna elements. However, modern automotive radars have MIMO arrays with 8 - 12 virtual elements and thus it might be better to create a new estimator that could work better with a small array.

5.5. Conclusion

This chapter shows that it is possible to relate the variance of the real part of a complex variable to the phase of the same complex variable directly. The phase variance can be estimated to the beam pointing error; the error that describes how large the shift is in location of the peak of the main beam. The estimation is only valid for small variances in phase errors and for a large number of antenna elements. Finding the peak of the main beam is done by looking at the antenna pattern and to avoid a large computation there will be a fast and unbiased interpolation to find the location of the peak.

The analytical expression and the cutoff point can be used to make the decision about the array permanence: for small calibration error, the beam-pointing can be assumed Gaussian, while for large calibration error, the main beam is distorted and has non-liner dependency on the calibration error.

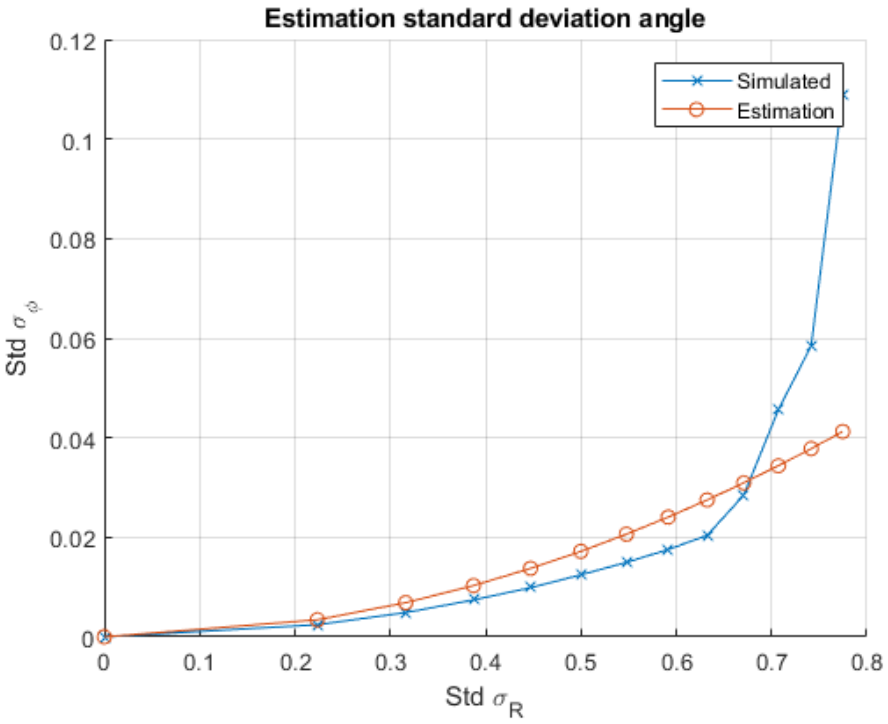

Figure 5.4: Estimation of std ϕ versus simulated standard deviation

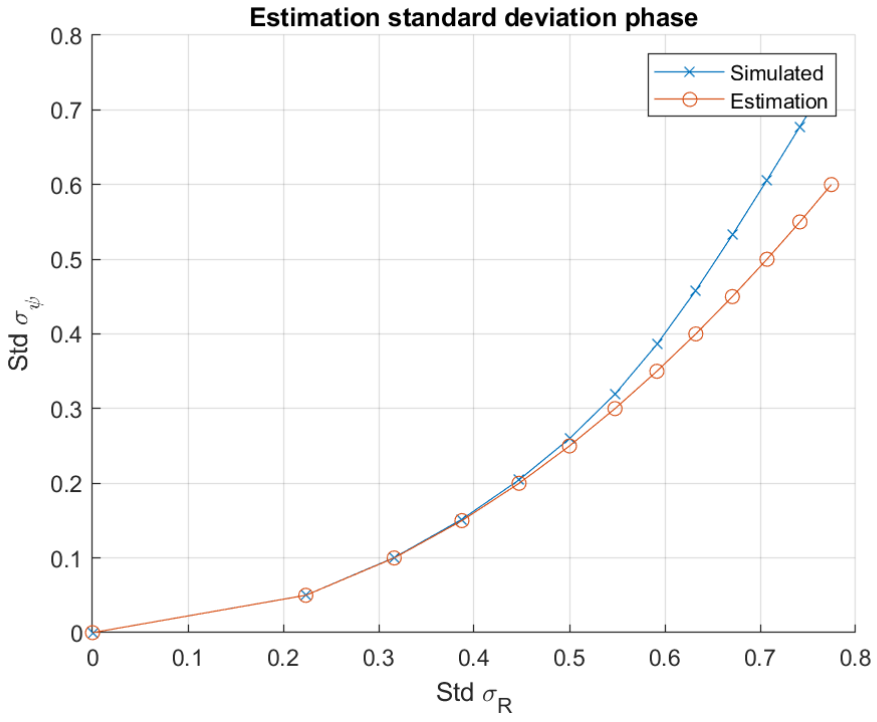

Figure 5.5: Estimation of larger number of antenna elements

6

Joint SLAM and calibration

This chapter will introduce the concepts of SLAM and the Extended Kalman Filter as they are described in literature and go into how this is usually applied for robotics. It will then extend from this technical framework and see how this might be used to jointly estimate the phase array calibration as well.

To perform the radar calibration the method without mutual coupling from chapter 4 will be included. The calibration techniques requires relative location of the targets and the radar to be known. In absence of calibration error, this problem is solved with SLAM techniques.

In this chapter, the framework of joint simultaneous localisation, mapping and calibration is introduced. The EKF SLAM modification for simultaneous calibration is proposed and its performance is assessed via numerical simulations.

6.1. Theory of SLAM

Simultaneous Localisation And Mapping (SLAM) techniques are useful to keep track of both the location of the radar and the objects of opportunity (or landmarks) at the same time. These two problems are linked and it is impossible to solve them independently from each other. Therefore this is often called a chicken and egg problem. It is technique that is often used in probabilistic robotics [32] [29] and is described by many papers [12], [3]. This is a statistical approach where the beliefs about the robot pose are represented as probability density functions.

The observations of the robot and the robot's controls are known and from this the robot tries to estimate the map of the environment and the path that the robot itself is taken. As the location of the radar and of the landmarks are dependent on each other there will be more uncertainty added to the system with each timestep. This uncertainty can only be resolved by an external calibration of one of the locations.

There are two steps that need to be taken to update both the radar's location and the environment. During the prediction step the radar tries to estimate it's predicted next location through his patter of predicted motion. In this step the uncertainty increases as the radar can only estimate where it will go. The predicted location is based on the previous measurement and radar pose and the control inputs. The uncertainty perpendicular to the movement grows much faster than in the direction of movement. This stems from the integration of the uncertainty about the radar's orientation.

The second step is the measurement or correction step, because the radar's location is updated after this step. The correction is based on the measurements it has received in this timestep. The radar uses the information from the landmarks in its environment to verify the location it has predicted in the previous step. The radar uses the information from the target landmarks in range to shrink the uncertainty that it has about its own predicted position.

The EKF allows for the transitions to be nonlinear functions. It linearises the nonlinear function around the estimate of the current mean and covariance of the system. That means

that the system is only viable in this linearisation point and this point needs to be recalculated at every timestep.

6.1.1. Probabilistic model for SLAM

The probabilistic model of standard SLAM problem (e.g. [12]) can be described in the following way.

The pdf that needs to be computed at every timestep t describes the joint distribution of all of the variables in the following way:

$$P(\boldsymbol{x}_t, \boldsymbol{m} | \boldsymbol{Z}_{0:t}, \boldsymbol{U}_{0:t}, \boldsymbol{x}_0) \tag{6.1}$$

Here $\boldsymbol{Z}_{0:t}$ is the set of all measurements, $\boldsymbol{U}_{0:t}$ all the control inputs to the radar that are used for prediction of its movement and $\boldsymbol{x}_0$ which is the initial position of the radar. These are all used to create the joint distribution of the current observation $\boldsymbol{x}_t$ and set of all landmarks $\boldsymbol{m}$.

This means that the calibration matrix that needs to be estimated is just a diagonal matrix. There are M antenna elements and thus as many calibration coefficients to be estimated. In presence of calibration error, the observed data depends on the relative positions of the landmarks and the radar, as well as the calibration coefficients.

Observation model

$$P(\boldsymbol{z}_t | \boldsymbol{x}_t, \boldsymbol{m}) \tag{6.2}$$

Motion model

$$P(\boldsymbol{x}_t | \boldsymbol{x}_{t-1}, \boldsymbol{u}_t) \tag{6.3}$$

Given probabilities 6.3.1 and 6.3.1, the joint probability 6.3.1 can be computed in a standard two-step recursive (sequential) prediction (time-update) correction (measurement-update) form

Prediction step

$$P(\boldsymbol{x}_t, \boldsymbol{m} | \boldsymbol{Z}_{0:t-1}, \boldsymbol{U}_{0:t}, \boldsymbol{x}_0) = \int P(\boldsymbol{x}_t | \boldsymbol{x}_{t-1}, \boldsymbol{u}_t) x P(\boldsymbol{x}_{t-1}, \boldsymbol{m} | \boldsymbol{Z}_{0:t-1}, \boldsymbol{U}_{0:t-1}, \boldsymbol{x}_0) d\boldsymbol{x}_{t-1} \tag{6.4}$$

Correction step

$$P(\boldsymbol{x}_t, \boldsymbol{m} | \boldsymbol{Z}_{0:t}, \boldsymbol{U}_{0:t}, \boldsymbol{x}_0) = \frac{P(\boldsymbol{z}_t | \boldsymbol{x}_t, \boldsymbol{m}, P(\boldsymbol{x}_t, \boldsymbol{m} | \boldsymbol{Z}_{0:t-1}, \boldsymbol{U}_{0:t}, \boldsymbol{x}_0)}{P(\boldsymbol{z}_t | \boldsymbol{Z}_{0:t-1}, \boldsymbol{U}_{0:t})} \tag{6.5}$$

6.2. Theory of Extended Kalman Filter

There are several ways in which this SLAM problem can be solved. In our case the algorithm that was chosen to solve the SLAM problem is the Extended Kalman Filter (EKF); the non-linear version of the Kalman filter [32]. The Kalman filter uses all previous measurements to estimate the next step of the system. All probability functions that are used to update the car's configuration are assumed to be Gaussian in the Kalman filter. This is appropriate in our case as all of the relevant factors are assumed to follow Gaussian distributions.

According to chapter 13 of [17] the extended Kalman filter can be used when the state equation and or observation equation is nonlinear. It linearises the system around a linearisation point in the system and then applies a Kalman filter. This makes it so that the system is only valid in this linearisation point. When the radar moves the system will need to be relinearised around the new radar pose. This makes it an iterative process.

The update equations for both the state and observation equations of the EKF are described in the book of Kay [17] as such:

$$\boldsymbol{s}[n] = \boldsymbol{a}(\boldsymbol{s}[n-1]) + \boldsymbol{B}\boldsymbol{u}[n] \tag{6.6}$$

$$\boldsymbol{x}[n] = \boldsymbol{h}(\boldsymbol{s}[n-1]) + \boldsymbol{w}[n] \tag{6.7}$$

Here $\boldsymbol{s}$ is the vector which describes the state equations of size $px1$ and where x is the vector which describes the measurement or observations equations. Looking at the sizes of the parts it can be seen that $\boldsymbol{a}$ is a p-dimensional and time-varying function and $\boldsymbol{B}$ is a known $p \times r$ matrix. The vector $\boldsymbol{u}$ accounts for things like modelling errors and unforeseen inputs. It consists of zero mean white Gaussian noise with covariance matrix $\boldsymbol{Q}$. In the observation equation h is an M-dimensional function and $\boldsymbol{w}$ is the observation noise which consists of zero mean Gaussian noise with a variance of σ_n^2. The matrices $\boldsymbol{A}$ and $\boldsymbol{H}$ are the Jacobians of $\boldsymbol{a}$ and $\boldsymbol{h}$.

Both the state equation and the observation equations are nonlinear and therefore it is necessary to linearise both the $\boldsymbol{a}$ and $\boldsymbol{h}$ functions through using a first-order Taylor expansion. What is different from the normal Kalman filter equations is that the matrix $\boldsymbol{A}$ is now time-varying and both equations have known terms added to them.

Prediction:

$$\hat{\boldsymbol{s}}[n|n-1] = \boldsymbol{a}(\hat{\boldsymbol{s}}[n-1|n-1]) \tag{6.8}$$

Minimum prediction MSE matrix $p \times p$:

$$\boldsymbol{M}[n|n-1] = \boldsymbol{A}[n-1]\boldsymbol{M}[n-1|n-1]\boldsymbol{A}^T[n-1] + \boldsymbol{B}\boldsymbol{Q}\boldsymbol{B}^T \tag{6.9}$$

Kalman Gain matrix pxM:

$$\boldsymbol{K}[n] = \boldsymbol{M}[n|n-1]\boldsymbol{H}^T[n](\boldsymbol{C}[n] + \boldsymbol{H}[n]\boldsymbol{M}[n|n-1]\boldsymbol{H}^T)^{-1} \tag{6.10}$$

Correction:

$$\hat{\boldsymbol{s}}[n|n] = \hat{\boldsymbol{s}}[n|n-1] + \boldsymbol{K}[n](\boldsymbol{x}[n] - \boldsymbol{h}(\hat{\boldsymbol{s}}[n|n-1])) \tag{6.11}$$

Minimum MSE matrix pxp:

$$\boldsymbol{M}[n|n] = (\boldsymbol{I} - \boldsymbol{K}[n]\boldsymbol{H}[n])\boldsymbol{M}[n|n-1] \tag{6.12}$$

where the $\boldsymbol{A}[n-1]$ and $\boldsymbol{H}[n]$ can be linearised through the Taylor expansion:

$$\boldsymbol{A}[n-1] = \left.\frac{\partial \boldsymbol{a}}{\partial \boldsymbol{s}[n-1]}\right|_{\boldsymbol{s}[n-1]=\hat{\boldsymbol{s}}[n-1|n-1]} \tag{6.13}$$

$$\boldsymbol{H}[n] = \left.\frac{\partial \boldsymbol{h}}{\partial \boldsymbol{s}[n]}\right|_{\boldsymbol{s}[n]=\hat{\boldsymbol{s}}[n|n-1]} \tag{6.14}$$

The performance of the filter will rely on the accuracy of the linearisation. It is not possible to determine the performance beforehand as it is a dynamic estimation and there is a lot of unpredictability.

6.3. Including calibration estimation in EKF-SLAM

This section will include the modification of the EKF SLAM for radar calibration. Starting out with the probabilistic model and then moving on to some necessary modifications for the algorithm.

6.3.1. Probabilistic model used for joint calibration and SLAM

The probabilistic model of standard SLAM problem (e.g. [12]) has to be modified in presence of calibration error, which directly affect the measurement model.

The pdf that needs to be computed at every timestep t describes the joint distribution of all of the variables in the following way:

$$P(\boldsymbol{x}_t, \boldsymbol{m}, \boldsymbol{\gamma} | \boldsymbol{Z}_{0:t}, \boldsymbol{U}_{0:t}, \boldsymbol{x}_0) \tag{6.15}$$

Here $\boldsymbol{Z}_{0:t}$ is the set of all measurements, $\boldsymbol{U}_{0:t}$ all the control inputs to the radar that are used for prediction of its movement and $\boldsymbol{x}_0$ which is the initial position of the radar. These are all used to create the joint distribution of the current observation $\boldsymbol{x}_t$, set of all landmarks $\boldsymbol{m}$ and set of all calibration coefficients $\boldsymbol{\gamma}$.

This means that the calibration matrix that needs to be estimated is just a diagonal matrix. There are M antenna elements and thus as many calibration coefficients to be estimated. In presence of calibration error, the observed data depends on the relative positions of the landmarks and the radar, as well as the calibration coefficients.

Observation model

$$P(\boldsymbol{z}_t|\boldsymbol{x}_t,\boldsymbol{m},\boldsymbol{\gamma}) \tag{6.16}$$

Motion model is similar to conventional SLAM problem

$$P(\boldsymbol{x}_t|\boldsymbol{x}_{t-1},\boldsymbol{u}_t) \tag{6.17}$$

Given probabilities 6.3.1 and 6.3.1, the joint probability 6.3.1 can be computed in a standard two-step recursive (sequential) prediction (time-update) correction (measurement-update) form

Prediction step

$$P(\boldsymbol{x}_t,\boldsymbol{m},\boldsymbol{\gamma}|\boldsymbol{Z}_{0:t-1},\boldsymbol{U}_{0:t},\boldsymbol{x}_0) = \int P(\boldsymbol{x}_t|\boldsymbol{x}_{t-1},\boldsymbol{u}_t)xP(\boldsymbol{x}_{t-1},\boldsymbol{m},\boldsymbol{\gamma}|\boldsymbol{Z}_{0:t-1},\boldsymbol{U}_{0:t-1},\boldsymbol{x}_0)d\boldsymbol{x}_{t-1} \tag{6.18}$$

Correction step

$$P(\boldsymbol{x}_t,\boldsymbol{m},\boldsymbol{\gamma}|\boldsymbol{Z}_{0:t},\boldsymbol{U}_{0:t},\boldsymbol{x}_0) = \frac{P(\boldsymbol{z}_t|\boldsymbol{x}_t,\boldsymbol{m},\boldsymbol{\gamma})P(\boldsymbol{x}_t,\boldsymbol{m},\boldsymbol{\gamma}|\boldsymbol{Z}_{0:t-1},\boldsymbol{U}_{0:t},\boldsymbol{x}_0)}{P(\boldsymbol{z}_t|\boldsymbol{Z}_{0:t-1},\boldsymbol{U}_{0:t})} \tag{6.19}$$

6.3.2. Necessary modifications

Now this theory will be used in an implementation for the Extended Kalman Filter that tracks both the calibration coefficients and the SLAM localisation. It is not possible to directly estimate the calibration coefficients as there are a few problems that prevent from doing this.

The Extended Kalman filter assumes all values have an error that can be represented with a Gaussian distribution. However when estimating complex values the noise can only be represented by a complex Gaussian distribution. The simple solution to estimate calibration coefficient is to introduce two variables to be tracked separately: the real part and imaginary part of the calibration coefficients. This is a Complex Kalman Filter [11]. This will cause us to have need for $2M$ coefficients to be tracked in the state vector. The real and complex components now have noise parts that can be represented with just a Gaussian distribution.

The second problem that there is is that in our case the measurement data for the estimation for the calibration coefficients will depend on the calibration coefficients themselves. This makes it so that the measurement depends on the measurement and the standard Kalman filter does not account for this. The way to overcome this limitation is to perform relative calibration as in (see chapter 4) by assuming the reference element to be calibrated. Without loss of generality consider the 0-th element the reference, thus its calibration coefficient is always 1. This is why this does not need to be tracked in the state vector and only $2(M-1)$ values have to be dynamically estimated.

In the conventional SLAM, the radar measured the target bearing angles ϕ and uses that in the measurement update. However the data that is gathered for the estimation of the calibration coefficients also includes the bearing ϕ:

$$X_m = \gamma_m \alpha e^{j2\pi\frac{d}{\lambda}sin(\phi)m}, m = 1 \dots M \tag{6.20}$$

Because the exact dependency of ϕ and the calibration coefficients is unknown; it will be necessary to remove the equation of ϕ from the Kalman filter. It will remain important to estimate this variable in some way and therefore a new way will have to be found to circumvent this.

6.4. EKF for joint SLAM and calibration

In robotics the robot's controls and inputs are known and represented in the matrix u. In the radar case this information is usually not available and thus no such estimation can be made. This is why the variable v has been added to the radar pose. It is possible to make a prediction of the next location of the radar by knowing the radar's location, velocity and angle at which is travelling. This will replace the information about the robot controls in the matrix u.

$$1: \textbf{Extended Kalman Filter}(\boldsymbol{\mu}_{t-1}, \boldsymbol{\Sigma}_{t-1}, \boldsymbol{u}_t, \boldsymbol{z}_t)$$

$$2: \bar{\boldsymbol{\mu}}_t = g(\boldsymbol{u}_t, \boldsymbol{\mu}_{t-1})$$
$$3: \bar{\boldsymbol{\Sigma}}_t = \boldsymbol{G}_t \boldsymbol{\Sigma}_{t-1} \boldsymbol{G}_t^T + \boldsymbol{R}_t$$

$$4: \boldsymbol{K}_t = \boldsymbol{\Sigma}_t \boldsymbol{H}_t^T (\boldsymbol{H}_t \bar{\boldsymbol{\Sigma}}_t \boldsymbol{H}_t^T + \boldsymbol{Q}_t)^{-1}$$
$$5: \boldsymbol{\mu}_t = \bar{\boldsymbol{\mu}}_t + \boldsymbol{K}_t (\boldsymbol{z}_t - h(\bar{\boldsymbol{\mu}}_t))$$
$$6: \boldsymbol{\Sigma}_t = (\boldsymbol{I} - \boldsymbol{K}_t \boldsymbol{H}_t) \bar{\boldsymbol{\Sigma}}_t$$

$$7: return \boldsymbol{\mu}_t, \boldsymbol{\Sigma}_t$$

Where the state vector $\boldsymbol{\mu}$ and covariance matrix $\boldsymbol{\Sigma}$ are updated every iteration. Here $\boldsymbol{u}$ and $\boldsymbol{z}$ are the process and observation noise which are assumed to be Gaussian distributed with zero mean and covariance $\boldsymbol{Q}$ and $\boldsymbol{R}$. The variable $\boldsymbol{K}$ is the Kalman gain and $\boldsymbol{G}$ and $\boldsymbol{H}$ are the Jacobians of g and h; the nonlinear transition functions.

Here the algorithm is divided into two steps:

- Prediction step: line 2-3
- Correction step: line 4-6

These steps will be explained in the following sections.

6.4.1. State vector

The state vector μ consists of all variables that are estimated in the Kalman filter.

The first values of the state vector consists of the radar pose. This is described by four variables: $[xyv\theta]^T$. That is the location of the radar in 2D Cartesian coordinates (x, y), the radial velocity of the radar v_r and the angle θ between the radar and the direction in which the radar is driving. As an illustration there is Figure 6.1 which describes the geometry.

There are also $M-1$ real antenna calibration coefficients γ^R and $M-1$ imaginary antenna calibration coefficients γ^I to be estimated and the $2N$ other variables represent the landmark locations $[x_n y_n]$. For now data association is assumed to be resolved. That means that it is known beforehand which measurement belongs to which landmark and the number of landmarks is also known beforehand. The state vector always has a fixed length because of this. The total length of the state vector is of length $4 + 2(M-1) + 2N$.

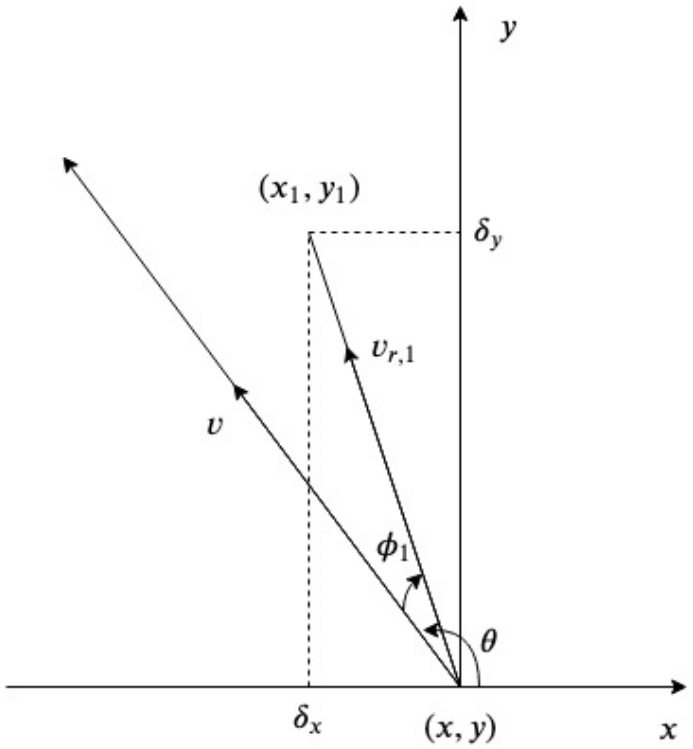

Figure 6.1: Illustration of used variables

$$\mu[t] = \begin{bmatrix} x \\ y \\ v \\ \theta \\ \gamma_1^R \\ \vdots \\ \gamma_{M-1}^R \\ \gamma_1^I \\ \vdots \\ \gamma_{M-1}^I \\ x_1 \\ y_1 \\ \vdots \\ x_N \\ y_N \end{bmatrix} \tag{6.21}$$

The covariance matrix Σ corresponding to the state vector is of size $(4+2(M-1)+2N)x(4+2(M-1)+2N)$. When there are for example eight antenna coefficients and ten landmarks to be estimated the state vector will be of length 38.

If the data association is not resolved and the number of landmarks are not known beforehand the state vector will be of unknown length. It is then possible to grow the state vector by extending it when a measurement from a new landmark is found.

6.4.2. Prediction step

In this step a prediction will be made and it will predict the next pose of the radar. The radar will move using the motion model g which is a constant velocity model.

$$g = \begin{bmatrix} x + vTcos(\theta) \\ y + vTsin(\theta) \\ v \\ \theta \end{bmatrix} \tag{6.22}$$

From the motion model it is possible to find the Jacobian $\boldsymbol{G}$ of the motion model that will be needed to update the covariance matrix $\boldsymbol{\Sigma}$. The Jacobian can be found by taking the first-order partial derivatives of all of the included variables:

$$\boldsymbol{G}_{1-4} = \begin{bmatrix} \frac{\partial g_1}{\partial x} & \frac{\partial g_1}{\partial y} & \frac{\partial g_1}{\partial v} & \frac{\partial g_1}{\partial \theta} \\ \frac{\partial g_2}{\partial x} & \frac{\partial g_2}{\partial y} & \frac{\partial g_2}{\partial v} & \frac{\partial g_2}{\partial \theta} \\ \frac{\partial g_3}{\partial x} & \frac{\partial g_3}{\partial y} & \frac{\partial g_3}{\partial v} & \frac{\partial g_3}{\partial \theta} \end{bmatrix} \tag{6.23}$$

Which results in the motion model:

$$\begin{bmatrix} x_t \\ y_t \\ \theta_t \\ v_k \end{bmatrix} = \begin{bmatrix} 1 & 0 & Tcos(\theta) & -vTsin(\theta) \\ 0 & 1 & Tsin(\theta) & vTcos(\theta) \\ 0 & 0 & 1 & 0 \\ 0 & 0 & 0 & 1 \end{bmatrix} \tag{6.24}$$

There is no prediction made for the change of the other variables and thus the Jacobian will just be the identity matrix for these variables. This causes the full Jacobian $\boldsymbol{G}$ to have the form:

$$G = \begin{bmatrix} \boldsymbol{G}_{1-4} & 0 \\ 0 & \boldsymbol{I}_{2(M-1)+2N} \end{bmatrix} \tag{6.25}$$

6.4.3. Correction step

In this step the prediction that was made is compared to the actual measurements and then updated in such a way that the smallest error is achieved.

The method for calculating the calibration coefficients γ were explained in the previous chapter 4. There are M calibration coefficients to be estimated, one for each antenna element, but as the data is normalised to the zeroth antenna element; there will be only $M-1$ coefficients that need to be tracked in the Kalman filter. As the real and imaginary parts of the coefficients are tracked separately this amount to $2(M-1)$ variables.

Recall from chapter 4 that in absence of coupling the ideal calibration coefficients γ can be calculated through this equation:

$$\gamma_m = \frac{s x_r^H}{x_r x_r^H} \tag{6.26}$$

The coefficients are gathered in the matrix $\Gamma = diag(\gamma)$. This will be just a diagonal matrix as there are no mutual coupling coefficients.

The data that is gathered for the estimation of the calibration coefficients is:

$$X_m = \gamma_m \alpha e^{j2\pi \frac{d}{\lambda} sin(\phi) m}, m = 0 \dots M-1 \tag{6.27}$$

Here α is the variable which relates to the SNR. The distance between the antenna elements d and the operating wavelength $\lambda = c/f$ and the angle ϕ which is the difference between the direction in which the radar is travelling and the landmark (see Figure 6.1). To reduce the dependency on the target magnitude, the normalised calibration coefficient is considered:

$$P_m = \frac{X_m}{X_0} = \frac{\gamma_m \alpha e^{j2\pi \frac{d}{\lambda} sin(\phi) m}}{\gamma_0 \alpha e^{j2\pi \frac{d}{\lambda} sin(\phi) 0}}, m = 1 \dots M-1 \tag{6.28}$$

$$P_m = \frac{X_m}{X_0} = \frac{\gamma_m}{\gamma_0} e^{j2\pi \frac{d}{\lambda} sin(\phi) m}, m = 1 \dots M-1 \tag{6.29}$$

This shows us that this function has now the following dependencies:

$$P = f(x, y, \theta, \gamma, x_N, y_N) \tag{6.30}$$

The equation for the normalised data can be simplified to just $M-1$ terms. Now the data will be split up in their real and imaginary parts to come to $2(M-1)$ elements that need to be tracked in the Kalman Filter.

There are several equations that are used to describe the Jacobian of the correction step. Now some auxiliary variables will be introduced to simplify the derivations:

Difference between current location of the radar and current location of the landmark

$$\delta = \begin{bmatrix} \delta_x \\ \delta_y \end{bmatrix} = \begin{bmatrix} \bar{\mu}_{r,x} - \bar{\mu}_{LM,x} \\ \bar{\mu}_{r,y} - \bar{\mu}_{LM,y} \end{bmatrix} \tag{6.31}$$

From this the squared Euclidean distance q between can be calculated

$$q = \delta^T \delta \tag{6.32}$$

Directly following from this is the range r to the target

$$r = \sqrt{q} \tag{6.33}$$

The radar measures the radial velocity of the target via Doppler processing (assume no Doppler ambiguities are present). The radial velocity v_r which describes the velocity vector that connects the radar and the current landmark.

$$v_r = v cos\phi \tag{6.34}$$

This description uses the bearing ϕ which is the angle between the direction the radar is travelling and the location of the landmark:

$$\phi = atan2(\delta_y, \delta_x) - \bar{\mu}_{R\theta} \tag{6.35}$$

Observation set

The algorithm looks at each detected target separately and for every target it will be possible to create a set of variables that describes the current observation. The predicted observation z consists of the range r to the target, the radial velocity v_r and the update to the calibration coefficients.

$$z = \begin{bmatrix} r \\ v_r \\ P_1^R \\ \vdots \\ P_{M-1}^R \\ P_1^I \\ \vdots \\ P_{M-1}^I \end{bmatrix} \tag{6.36}$$

6.4.4. Jacobian H

All of these factors are used in creating the Jacobian H, which is the matrix used to create the Kalman gain which will compare the observation z and the prediction $h(\bar{\mu}_t)$.

The matrix H can be split up into three distinct parts:

- $\boldsymbol{H}_{pose}$ relating to the position, angle and speed of the radar
- $\boldsymbol{H}_{gamma}$ relating to the calibration coefficients
- $\boldsymbol{H}_{landmark}$ relating to the observed landmarks

$$\boldsymbol{H} = \begin{bmatrix} \boldsymbol{H}_{pose} & \boldsymbol{H}_{gamma} & \boldsymbol{H}_{landmark} \end{bmatrix} \tag{6.37}$$

For readability $H_{landmark}$ is given for just one target. It should be repeated N times to include all landmarks.

$$\psi = j2\pi\frac{d}{\lambda}sin\phi \tag{6.38}$$

$$H_{pose} = \begin{bmatrix} \frac{\partial r}{\partial x} & \frac{\partial r}{\partial y} & \frac{\partial r}{\partial v} & \frac{\partial r}{\partial \theta} \\ \frac{\partial v_r}{\partial x} & \frac{\partial v_r}{\partial y} & \frac{\partial v_r}{\partial v} & \frac{\partial v_r}{\partial \theta} \\ \frac{\partial P_1^R}{\partial x} & \frac{\partial P_1^R}{\partial y} & \frac{\partial P_1^R}{\partial v} & \frac{\partial P_1^R}{\partial \theta} \\ \vdots & \vdots & \vdots & \vdots \\ \frac{\partial P_{M-1}^R}{\partial x} & \frac{\partial P_{M-1}^R}{\partial y} & \frac{\partial P_{M-1}^R}{\partial v} & \frac{\partial P_{M-1}^R}{\partial \theta} \\ \frac{\partial P_1^I}{\partial x} & \frac{\partial P_1^I}{\partial y} & \frac{\partial P_1^I}{\partial v} & \frac{\partial P_1^I}{\partial \theta} \\ \vdots & \vdots & \vdots & \vdots \\ \frac{\partial P_{M-1}^I}{\partial x} & \frac{\partial P_{M-1}^I}{\partial y} & \frac{\partial P_{M-1}^I}{\partial v} & \frac{\partial P_{M-1}^I}{\partial \theta} \end{bmatrix}$$

$$= \begin{bmatrix} \frac{-\sqrt{q}\delta_x}{q} & \frac{-\sqrt{q}\delta_y}{q} & 0 & 0 \\ \frac{\delta_y}{q} & \frac{-\delta_x}{q} & 0 & -1 \\ \gamma_1^R e^{1\psi} j2\pi\frac{d}{\lambda}1\frac{\delta_y}{q} & \gamma_1^R e^{1\psi} j2\pi\frac{d}{\lambda}1\frac{\delta_x}{q} & 0 & \gamma_1^R e^{1\psi} j2\pi\frac{d}{\lambda}1(-1) \\ \vdots & \vdots & \vdots & \vdots \\ \gamma_{M-1}^R e^{M\psi} j2\pi\frac{d}{\lambda}(M-1)\frac{\delta_y}{q} & \gamma_{M-1}^R e^{1\psi} j2\pi\frac{d}{\lambda}(M-1)\frac{\delta_x}{q} & 0 & \gamma_{M-1}^R e^{(M-1)\psi} j2\pi\frac{d}{\lambda}1(-1) \\ \gamma_1^I e^{1\psi} j2\pi\frac{d}{\lambda}1\frac{\delta_y}{q} & \gamma_1^I e^{1\psi} j2\pi\frac{d}{\lambda}1\frac{\delta_x}{q} & 0 & \gamma_1^I e^{1\psi} j2\pi\frac{d}{\lambda}1(-1) \\ \vdots & \vdots & \vdots & \vdots \\ \gamma_{M-1}^I e^{M\psi} j2\pi\frac{d}{\lambda}(M-1)\frac{\delta_y}{q} & \gamma_{M-1}^I e^{1\psi} j2\pi\frac{d}{\lambda}(M-1)\frac{\delta_x}{q} & 0 & \gamma_{M-1}^I e^{(M-1)\psi} j2\pi\frac{d}{\lambda}1(-1) \end{bmatrix}$$

$$\mathrm{H}_{gamma} = \begin{bmatrix} \frac{\partial r}{\partial \gamma_1^R} & \cdots & \frac{\partial r}{\partial \gamma_{M-1}^R} & \frac{\partial r}{\partial \gamma_1^I} & \cdots & \frac{\partial r}{\partial \gamma_{M-1}^I} \\ \frac{\partial v_r}{\partial \gamma_1^R} & \cdots & \frac{\partial v_r}{\partial \gamma_{M-1}^R} & \frac{\partial v_r}{\partial \gamma_1^I} & \cdots & \frac{\partial v_r}{\partial \gamma_{M-1}^I} \\ \frac{\partial P_1^R}{\partial \gamma_1^R} & \cdots & \frac{\partial P_1^R}{\partial \gamma_{M-1}^R} & \frac{\partial P_1^R}{\partial \gamma_1^R} & \cdots & \frac{\partial P_1^R}{\partial \gamma_{M-1}^R} \\ \vdots & \vdots & \vdots & \vdots & \vdots & \vdots \\ \frac{\partial P_{M-1}^R}{\partial \gamma_1^R} & \cdots & \frac{\partial P_{M-1}^R}{\partial \gamma_{M-1}^T} & \frac{\partial P_{M-1}^R}{\partial \gamma_1^I} & \cdots & \frac{\partial P_{M-1}^R}{\partial \gamma_{M-1}^I} \\ \frac{\partial P_1^I}{\partial \gamma_1^R} & \cdots & \frac{\partial P_1^I}{\partial \gamma_{M-1}^R} & \frac{\partial P_1^I}{\partial \gamma_1^R} & \cdots & \frac{\partial P_1^I}{\partial \gamma_{M-1}^R} \\ \vdots & \vdots & \vdots & \vdots & \vdots & \vdots \\ \frac{\partial P_{M-1}^I}{\partial \gamma_1^R} & \cdots & \frac{\partial P_{M-1}^I}{\partial \gamma_{M-1}^R} & \frac{\partial P_{M-1}^I}{\partial \gamma_1^I} & \cdots & \frac{\partial P_{M-1}^I}{\partial \gamma_{M-1}^I} \end{bmatrix}$$

$$= \begin{bmatrix} 0 & \dots & \dots & \dots & \dots & 0 \\ 0 & \dots & \dots & \dots & \dots & 0 \\ cos\psi 1 & 0 & 0 & -sin\psi 1 & 0 & 0 \\ 0 & \ddots & 0 & 0 & \ddots & 0 \\ 0 & 0 & cos\psi(M-1) & 0 & 0 & -sin\psi(M-1) \\ sin\psi 1 & 0 & 0 & cos\psi 1 & 0 & 0 \\ 0 & \ddots & 0 & 0 & \ddots & 0 \\ 0 & 0 & sin\psi(M-1) & 0 & 0 & cos\psi(M-1) \end{bmatrix}$$

$$\mathrm{H}_{landmark_i} = \begin{bmatrix} \frac{\partial r}{\partial x_i} & \frac{\partial r}{\partial y_i} \\ \frac{\partial v_r}{\partial x_i} & \frac{\partial v_r}{\partial y_i} \\ \frac{\partial P_1^R}{\partial x_i} & \frac{\partial P_1^R}{\partial y_i} \\ \vdots & \vdots \\ \frac{\partial P_{M-1}^R}{\partial x_i} & \frac{\partial P_{M-1}^R}{\partial y_i} \\ \frac{\partial P_1^I}{\partial x_i} & \frac{\partial P_1^I}{\partial y_i} \\ \vdots & \vdots \\ \frac{\partial P_{M-1}^I}{\partial x_i} & \frac{\partial P_{M-1}^I}{\partial y_i} \end{bmatrix}$$

$$= \begin{bmatrix} \frac{\sqrt{q}\delta_x}{q} & \frac{\sqrt{q}\delta_y}{q} \\ \frac{-\delta_y}{q} & \frac{\delta_x}{q} \\ \gamma_1^R e^{1\psi} j2\pi \frac{d}{\lambda} 1 \frac{-\delta_y}{q} & \gamma_1^R e^{1\psi} j2\pi \frac{d}{\lambda} 1 \frac{\delta_x}{q} \\ \vdots & \vdots \\ \gamma_{M-1}^R e^{M\psi} j2\pi \frac{d}{\lambda}(M-1) \frac{-\delta_y}{q} & \gamma_{M-1}^R e^{1\psi} j2\pi \frac{d}{\lambda}(M-1) \frac{\delta_x}{q} \\ \gamma_1^R e^{1\psi} j2\pi \frac{d}{\lambda} 1 \frac{-\delta_y}{q} & \gamma_1^R e^{1\psi} j2\pi \frac{d}{\lambda} 1 \frac{\delta_x}{q} \\ \vdots & \vdots \\ \gamma_{M-1}^R e^{M\psi} j2\pi \frac{d}{\lambda}(M-1) \frac{-\delta_y}{q} & \gamma_{M-1}^R e^{1\psi} j2\pi \frac{d}{\lambda}(M-1) \frac{\delta_x}{q} \end{bmatrix}$$

Combining these matrices gives the transition matrix H which is of size $(3+M)x(4+2N+M)$ = $11x14$ when one target is observed.

The derivations of the matrix H are described in Appendix A.

6.4.5. Problem with implementation for uncalibrated array

This implementation for SLAM will work when the array is properly calibrated.

$$\hat{\phi}_{CAL} \sim \mathcal{N}(\phi_0, \sigma_\phi^2) \tag{6.42}$$

When this is the case the maximum of the antenna pattern will point in the right direction. However when there is an error in beam-pointing, as was described in chapter 5, it will no longer be possible to accurately predict the bearing ϕ. This error occurs when the antenna pattern is not properly calibrated.

This beam-pointing error causes a problem with this implementation of the Extended Kalman Filter as now this parameter will not be able to be represented by a Gaussian distribution:

$$\hat{\phi}_{UNCAL} \sim \mathcal{N}(\phi_0, \sigma_\phi^2) \tag{6.43}$$

As was mentioned earlier in the chapter this Gaussian assumption is a requirement for the Kalman Filter. This equation for ϕ is used when initialising a target and this will be explained in depth in the next section.

6.5. Target initialisation

When the target is observed for the first time, its location should be initialised. If the array is poorly calibrated at this moment, the wrong initialisation can significantly degrade the overall SLAM performance.

The bearing ϕ that is used during target initialisation can no longer be assumed Gaussian distributed in all cases. To circumvent this there are multiple equations that can describe the bearing ϕ by using variables that will still be tracked in the filter. The equations will be used when adding information about a new landmark to the state vector and as an auxiliary variable when calculating the Jacobian $\boldsymbol{H}$.

There are two estimators for ϕ: one based on the (calibrated) antenna pattern and one on the estimate for Doppler velocity. It will also be possible to combine both into new estimator that is a weighted combination of both. To implement this estimator it will be necessary to make an estimate of the variance for both of these estimators.

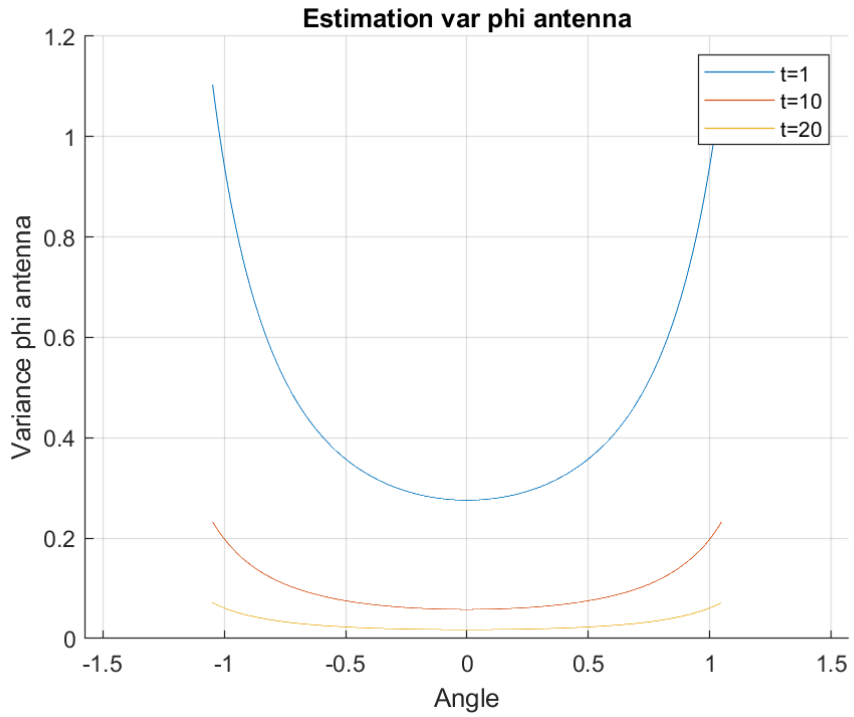

Figure 6.2: Estimation of variance $\phi_{antenna}$ for different timesteps

6.5.1. Phase array estimation

The first estimator ϕ_{ant} is based on the antenna pattern and the current estimate of the calibration coefficients. The spike of the calibrated antenna pattern should be in the direction of the main beam.

$$\hat{\phi}_{antenna} = \arg\max_{\phi} \left(\frac{\boldsymbol{a}^H \boldsymbol{P}_m}{\boldsymbol{a}\boldsymbol{a}^H} \right) \tag{6.44}$$

Here $\boldsymbol{a}$ is the ideal steering vector for every angle ϕ of the target and P_m is the normalised calibration data; this time however the normalised first element is of course still used to recreate the antenna pattern:

$$P = [1P_1 \dots P_{M-1}]^T \tag{6.45}$$

Chapter 5 mentions that in presence of calibration errors the estimator for ϕ_{ant} will only be valid when the variance is in the operating region. It will be best to assign a very large variance outside the operating region.

$$\hat{\phi}_{ant} = \begin{cases} \hat{\phi}_{ant} & \sigma_R^2 < \alpha \\ +\infty & \sigma_R^2 > \alpha \end{cases} \tag{6.46}$$

Variance phase array estimation

As was discussed in chapter 5 it will be possible to use the estimation that relates the variance of the real part of a complex random variable to the phase error distribution.

Taking the combined equation from this chapter:

$$\sigma_{\phi_{ant}}^2 = \frac{2(3)^{1/2}\sigma_R^2}{kdcos\theta_0(M-1)^{3/2}} \tag{6.47}$$

This estimation can be used only when the variance of the calibration coefficients σ_R^2 will be smaller than the cut off point α. For a larger calibration error, the main beam is distorted and angular measurements with the array do not bring useful information.

Figure 6.2 shows the estimation of the variance $\phi_{antenna}$ at different timesteps in the algorithm and it is visible that the variance decreases as time goes on.

6.5.2. Doppler beam sharpening

Looking at ϕ_{dop} it is based on the geometry of the current estimation for velocity v that will be given by the radar and Doppler radial velocity v_r:

$$\phi_{doppler} = \pm acos\left(\frac{v_r}{v}\right) \tag{6.48}$$

Using this equations brings two problems with it that need to be solved.

Firstly the acos has a range of angles between $[0, \pi]$ radian. The problem in this implementation is that it adds angle ambiguity as there are two angles that give the same result. So even if the algorithm is capable of determining at which angle the new landmark is located it cannot determine whether the target will be located on the left or the right side of the radar.

This problem can be be circumvented by using another equation for ϕ to solely determine the sign ω that the angle should be assigned to when initialising a new target. This equation is based on the current estimation of the calibration coefficients Γ:

$$\omega = sign(\arg\max_{\phi} \mathcal{F}\{\Gamma^{-1}P\}) \tag{6.49}$$

This relies on the fact that antenna pattern is able to distinguish between the targets on the right an on the left, and the targets are stationary. This initialisation will ensure that the correct side of the radar is chosen very accurately for landmarks that are initialised after this.

The second problem with the formula for ϕ_{dop} arises when the angle is located close to the direction of the radar movement. In this case it might happen that the ratio of the estimated radial velocity v_r and the estimated radar velocity v is larger than one. The acos again does not account for this as the results of outputs outside of the range of $[-1, 1]$ will produce an imaginary result.

This problem will be avoided in two ways: by trying to choose the targets of opportunity to not appear too close the direction the radar is travelling and by assigning a very large variance to the estimator ϕ_{dop} when the ratio is larger than one.

$$\hat{\phi}_{dop} = \begin{cases} \hat{\phi}_{dop} & \frac{v_r}{v} < 1 \\ +\infty & \frac{v_r}{v} > 1 \end{cases} \tag{6.50}$$

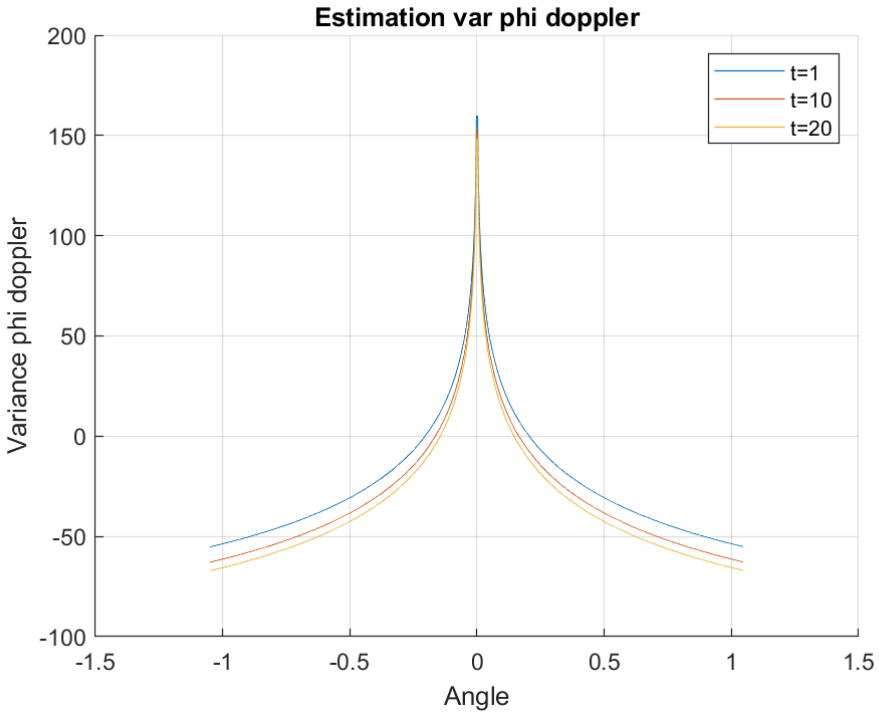

Figure 6.3: Estimation of variance $\phi_{doppler}$ for different timesteps

Variance Doppler beam sharpening

Since ϕ_{dop} is the transformation of the other measured variables - v_r and v in equation 6.5.2, its variance can be found using the rule of variables transformation [17]. ϕ_{dopp} can be expressed as a function g of v_r:

$$\phi_{dopp} = g(v_r) \tag{6.51}$$

However the book states that ”the efficiency of an estimator is destroyed by a nonlinear transformation” and as this relation is described by a nonlinear function the estimator will not be efficient. It is however ”approximately maintained over nonlinear transformations if the data record is large enough”.

It is possible to find the variance for ϕ_{dop} in this way:

$$\sigma^2_{\phi_{doppler}} \geq \frac{(\frac{\partial g}{\partial v_r})^2}{-E\left[\frac{\partial^2 lnp(x;\phi)}{\partial^2 \phi^2}\right]} \tag{6.52}$$

Here the denominator is described as the Fisher information matrix $I(\phi)$.

If the velocity of the radar is known explicitly, and CRB of the Doppler measurement is known this can be found by using the following derivations:

$$\frac{\partial \sigma^2_{\phi_{doppler}}}{\partial v_r} = \frac{-1}{\sqrt{1-(\frac{v_r}{v})^2 v^2}} \tag{6.53}$$

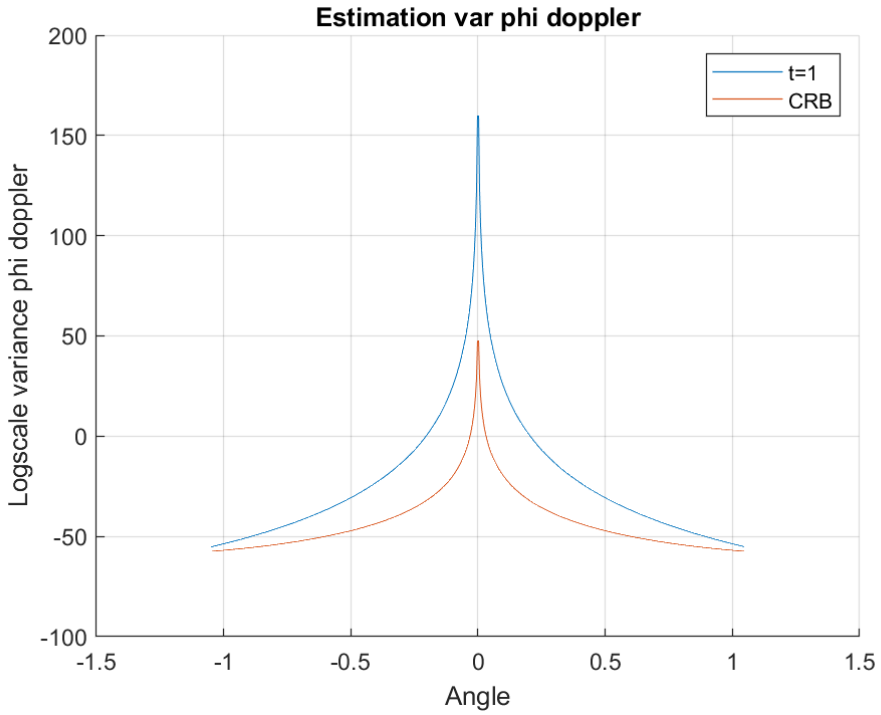

Figure 6.4: Estimation of variance $\phi_{doppler}$ with the CRB included

$$\left(\frac{\partial g}{\partial v_r}\right)^2 = \frac{1}{v^2(1-(\frac{v_r}{v})^2)} \tag{6.54}$$

To sum it up the variance can be described in the following way:

$$\sigma^2_{\phi_{doppler}} \geq \frac{\sigma_R^2}{v^2(1-(\frac{v_r}{v})^2)} \tag{6.55}$$

Figure 6.3 shows the variance at different time instances. The y-axis is shown on a logarithmic scale. The variance decreases as time goes on. In this example the variance is explicitly chosen small so the algorithm never goes out of the operating region.

In reality, the exact velocity of the radar is unknown, but rather estimated in the SLAM with the variance σ_v^2. Taking this into account, the accuracy of angular measurements with Doppler beam-sharpening is:

$$\sigma_\phi^2 = \frac{\partial g(\phi)}{\partial \phi} I^{-1}(\phi) \frac{\partial g(\phi)^T}{\partial \phi} \tag{6.56}$$

$$I^{-1}(\phi) = \begin{bmatrix} \sigma_{v_r} & 0 \\ 0 & \sigma_v \end{bmatrix} \tag{6.57}$$

Jacobian matrix g:

$$\frac{\partial g}{\partial \phi} = \begin{bmatrix} \frac{\partial g_1}{\partial v_r} \\ \frac{\partial g_2}{\partial v} \end{bmatrix} \tag{6.58}$$

$$\frac{\partial g_1}{\partial v_r} = \frac{-1}{\sqrt{1-(\frac{v_r}{v})^2}v} \tag{6.59}$$

$$\frac{\partial g_2}{\partial v} = \frac{v_r}{\sqrt{1-(\frac{v_r}{v})^2 v^2}} \tag{6.60}$$

This allows us to make a combined analytical expression:

$$\sigma^2_{\phi_{doppler}} = \left(\frac{-1}{\sqrt{1-(\frac{v_r}{v})^2 v}} + \frac{v_r}{\sqrt{1-(\frac{v_r}{v})^2 v^2}}\right)\left(\sigma_{v_r}\frac{-1}{\sqrt{1-(\frac{v_r}{v})^2 v}} + \sigma_v \frac{v_r}{\sqrt{1-(\frac{v_r}{v})^2 v^2}}\right) \tag{6.61}$$

Figure 6.4 shows the estimator for $\phi_{doppler}$ together with the CRB. The y-axis of the figure is shown in logaritmic scale. It can be seen that the estimated variance has a shape similar to the CRB, but it remains always larger.

6.5.3. Combined estimator

Currently there are two estimators for ϕ; as both of them have their own advantages and disadvantages a weighted least squares (WLS) estimator will be used to combine them both to create a better estimator. The weighted least squares error (WLS) [17] that will be used can be described as follows:

$$\hat{\phi}_{WLS} = \frac{\frac{\hat{\phi}_{dop}}{\sigma^2_{\phi_{dop}}} + \frac{\hat{\phi}_{ant}}{\sigma^2_{\phi_{ant}}}}{\frac{1}{\sigma^2_{\phi_{dop}}} + \frac{1}{\sigma^2_{\phi_{ant}}}} \tag{6.62}$$

To summarise the total estimator for ϕ can be used in these cases:

$$\hat{\phi} = \begin{cases} \hat{\phi}_{antenna} & \sigma_R^2 < \alpha, \frac{v_r}{v} > 1 \\ \hat{\phi}_{WLS} & \sigma_R^2 < \alpha, \frac{v_r}{v} < 1 \\ \hat{\phi}_{doppler} & \sigma_R^2 > \alpha, \frac{v_r}{v} < 1 \\ 0 & \sigma_R^2 > \alpha, \frac{v_r}{v} > 1 \end{cases} \tag{6.63}$$

The problem here is that there is one case for which there is no estimator. This case will be very unlikely as we assume that the radar will be in the operating region ($\sigma_R^2 < \alpha$) when it is initially calibrated. If this is not the case and a target does appear close to the radar where $\frac{v_r}{v} > 1$ it would be best to skip over such a target and wait until the target is detected at a different angle by the radar.

6.6. Images from algorithm

This section will provide some snapshots that show how the joint SLAM and calibration works. Table 6.1 describes the variables that were used to create these images.

In the rest of this chapter there are images that show how the algorithm estimates the calibration coefficients.

In Figure 6.5 the algorithm is initialised. The radar starts at (0,0) and is represented by the blue circle. The red shape shows at what range the radar detects the landmarks. The landmarks are shown by black crosses and when a landmark is detected by the radar a black line is shown towards the prediction. The black circles show where the radar predicts that the landmark is located. The blue ellipse that is shown represents the uncertainty that surrounds this landmark.

In Figure 6.6 the antenna pattern is initialised. The first estimated red pattern will start at the blue distorted pattern. The ideal antenna pattern is given in black. The calibration coefficients are randomly generated, but are assumed to always be degrading: $|C| < 1$

In the following Figures 6.7 until 6.18 the algorithm will converge to an estimation for the calibration pattern that is comparable to the ones given in chapter 4. The algorithm converges quickly and even a landmark that is not correctly placed will not degrade the pattern that badly.

M	8
N	10
f	77 GHz
d	$\lambda/2$
Radar range	50 m
Radar view	$[\pi/3, \pi/3]$
Velocity v	10 m/s
Refresh rate T	10 Hz
Target SNR	30 dB
Calibration coefficients	Degrading $C_{ij} \sim \mathcal{N}(0.6, 0.1)$
σ_x	10^{-4}
σ_y	10^{-4}
σ_v	0.1
σ_θ	10^{-6}
σ_γ	0.1
σ_R	0.15

Table 6.1: Table that includes the variables used in the EKF

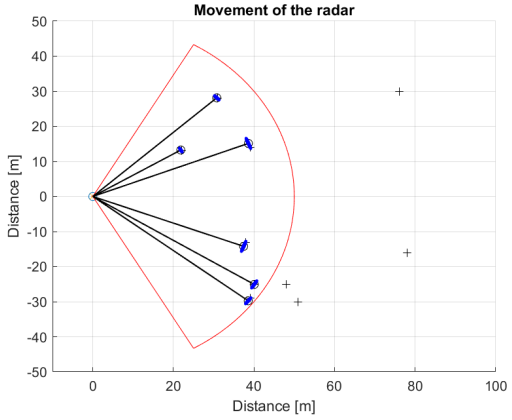

Figure 6.5: Initialisation radar map

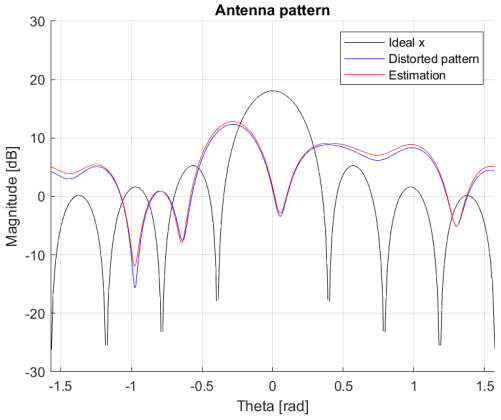

Figure 6.6: Initialisation pattern estimation

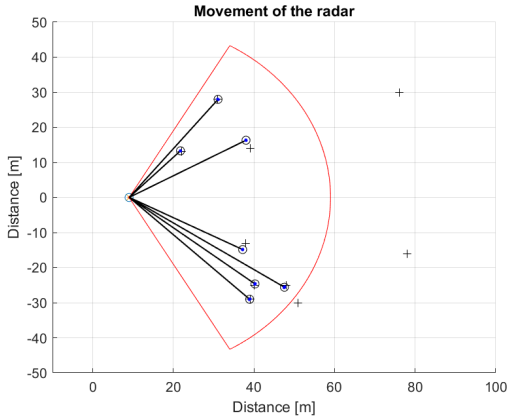

Figure 6.7: T=10 radar map

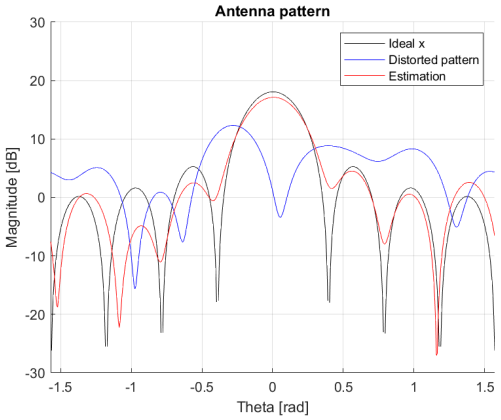

Figure 6.8: T=10 pattern estimation

6.6.1. Wrong angle

Figures 6.19 until 6.22 show what the effects of choosing the wrong side for the angle can be. In the initialisation there are only two landmarks in range and this appears to not have been enough to make a good decision on whether or not the landmark needs to be initialised on the left or on the right. The wrong angle was chosen and there are a lot of errors introduced

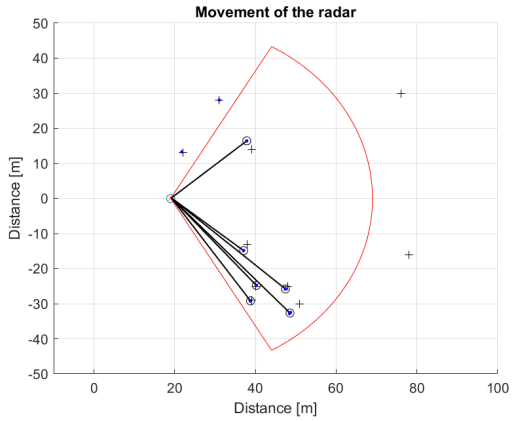

Figure 6.9: T=20 radar map

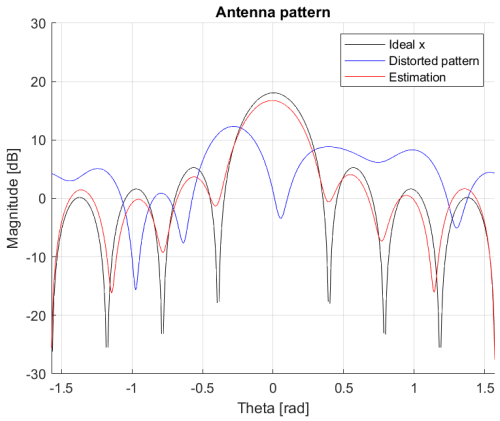

Figure 6.10: T=20 pattern estimation

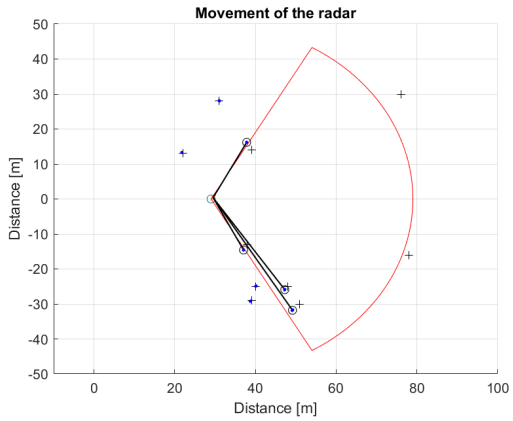

Figure 6.11: T=30 radar map

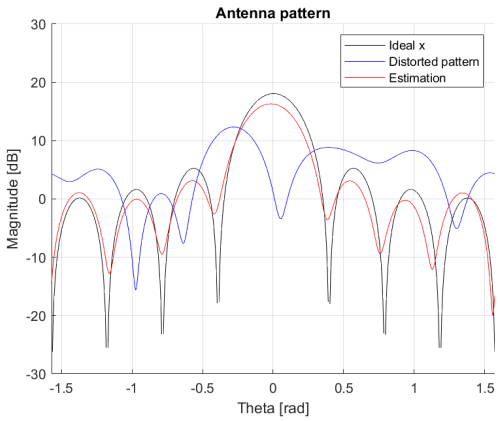

Figure 6.12: T=30 pattern estimation

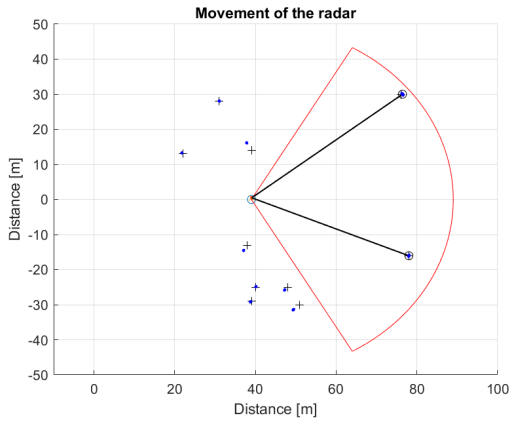

Figure 6.13: T=40 radar map

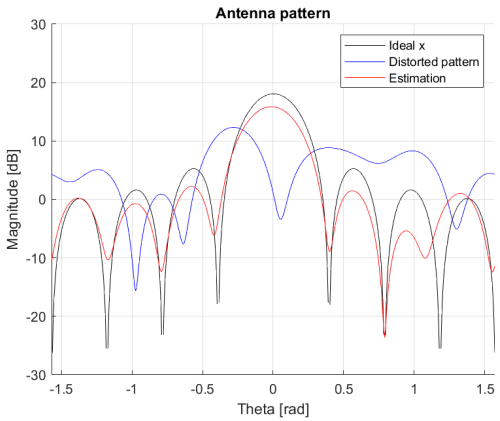

Figure 6.14: T=40 pattern estimation

in the pattern that will (most likely) not be recovered.

6.7. Verification of the combined estimation

To look at how good the estimation of the calibration coefficients is performing the covariance matrix Σ will be analysed. The matrix keeps track of the uncertainty of all of the coefficients, but what is most important in this case is how well the calibration coefficients are performing. That is why the variance of the coefficients will be an important metric. This is done by

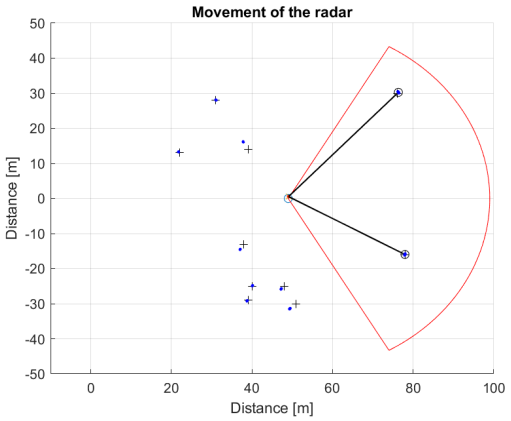

Figure 6.15: T=50 radar map

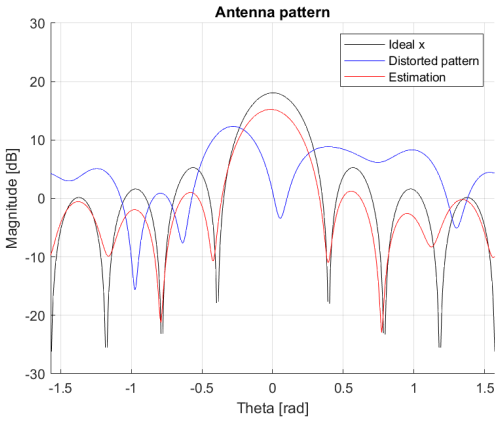

Figure 6.16: T=50 pattern estimation

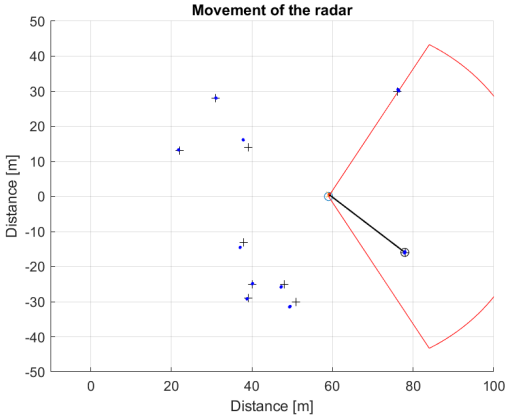

Figure 6.17: T=60 radar map

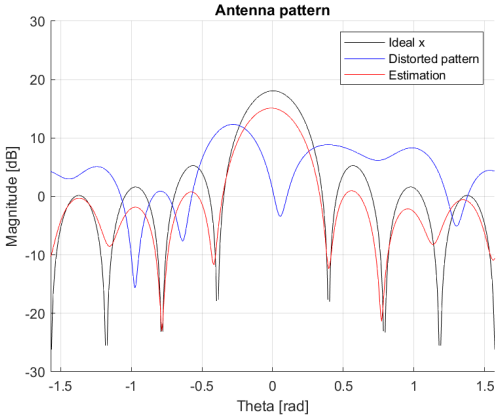

Figure 6.18: T=60 pattern estimation

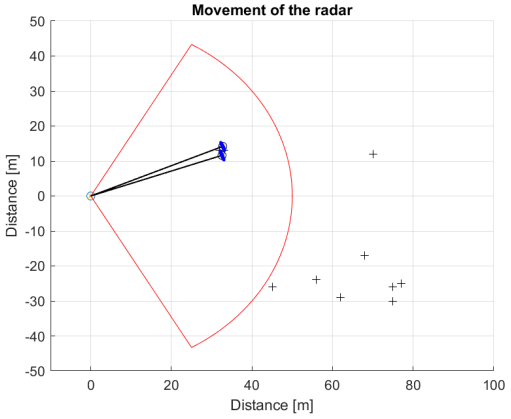

Figure 6.19: Initialisation radar map

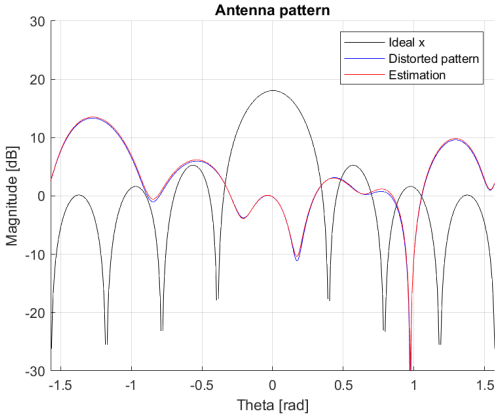

Figure 6.20: Initialisation pattern estimation

taking the sum of all of the elements on the diagonal matrix that pertain to the calibration coefficients:

$$\sigma_\gamma^2 = \frac{1}{M} trace[\Sigma_\gamma] \tag{6.64}$$

This is the combination of the variances of the real and imaginary parts of the calibration coefficients, but how these parts can be combined is described in a previous chapter.

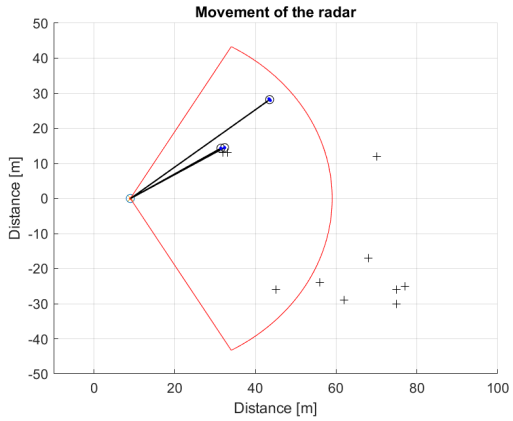

Figure 6.21: T=10 radar map

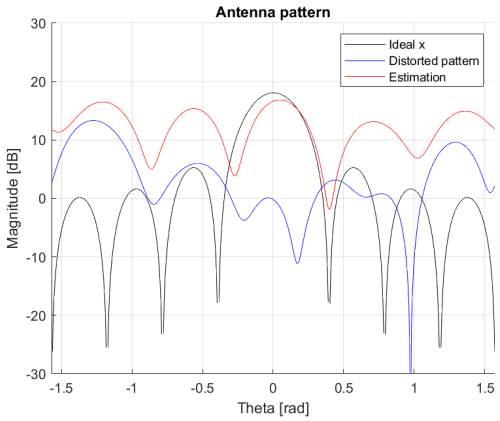

Figure 6.22: T=10 pattern estimation

Now looking at the variance and the number of antenna elements in Figure 6.23 there is a clear relation. The more antenna elements there are the larger the variance of the calibration coefficients. This is because the larger the number of antenna elements the larger the number of coefficients that need to be estimated and the more mistakes can be made in calibration.

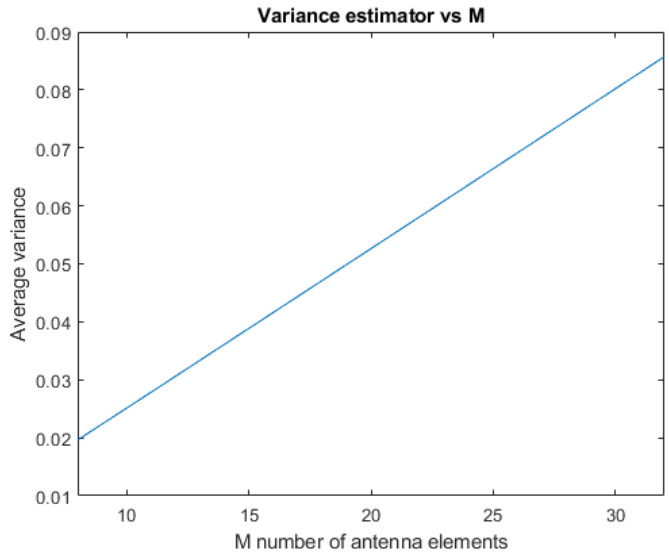

Figure 6.23: Variance against number of antenna elements M

It is also possible to look at the effect of the number of targets to the variance in Figure 6.24. For this the number of targets has been varied by lowering the distance between targets each time; effectively increasing the target density. It is clear the the variance decreases when the number of targets increases. Using more data will give a better pattern shape, even when the landmark is estimated in the wrong location.

The algorithm does not converge when we are not in the working region of calibration and the observed targets are in front of the radar.

6.8. Conclusion

This chapter discusses the implementation of the modification of SLAM to the joint problem of SLAM + calibration.

It is necessary to track the real and imaginary part of the calibration coefficients separately in the Kalman filter as the filter assumes that all the distributions that are used are Gaussian.

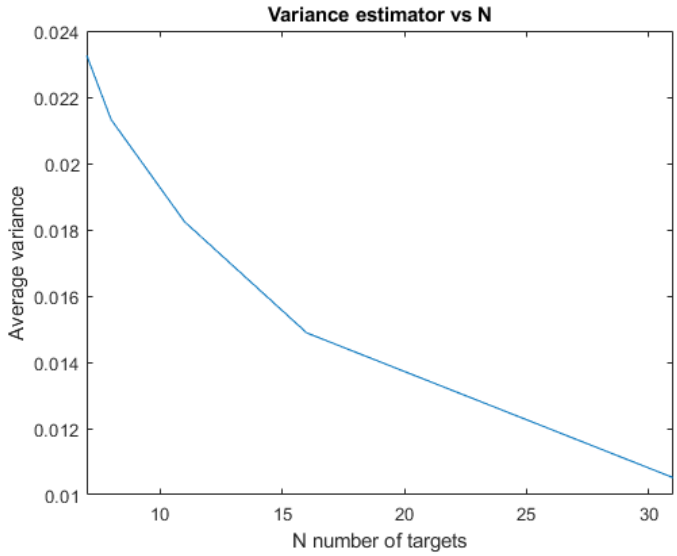

Figure 6.24: Variance against number of targets N

The dependency on the absolute target magnitude is solved by normalising the calibration coefficients first to the first element. This also allows use to skip the estimation of the first calibration coefficients; lowering the number of elements that need to be tracked in the filter. The measured angle of the target in the standard slam is substituted with measurements of the full array response to perform calibration. This was necessary because the equation for the calibration coefficients depends on the calibration coefficients themselves and this is another situation that is not described by the Kalman filter.

The biggest problem that was solved relates to the bearing that was removed from the standard SLAM movement filter. The variable is however still necessary when adding new landmarks to the filter and thus it needs to be estimated using other variables that are still tracked in the filter.

The framework that was introduced works for a well calibrated array, but causes problems with an uncalibrated array. Therefore there are two different equations introduced that can estimate the bearing. Both of the estimators can be used under different conditions and they can even be combined into a weighted least squares estimator. To implement this an estimation was made of the variance of both estimators.

The algorithm needs reasonable estimation of calibration coefficients during the initialisation, otherwise the uncertainty in the calibration can lead to divergence of the whole SLAM + localisation. The algorithm has been shown to work when these operating conditions are met.

7

Conclusion

7.1. Conclusion

The goal of this thesis was to look at several situations and parameters that might influence the performance of the radar. The study within this thesis project has been divided into two main topics:

- to study the effects of adverse weather conditions on the statistics of observed radar targets characteristics
- to use objects of opportunity to estimate the calibration coefficients of a MIMO radar system

Adverse weather conditions

A statistical analysis was performed on datasets of stationary objects that were loosely divided into different weather conditions. A distinction was made between three weather conditions: normal weather, light rain and heavy rain. As the objects were stationary it was sufficient to use a nearest neighbour algorithm for data association.

There was a large variation to be detected during heavy rainfall within the course of the measurement. For a cylindrical target there was an increase in average RCS of about 0.7 dBsm2 within one heavy rain measurement. This shift is likely caused because of the location where the measurements were performed. During heavy rainfall puddles were formed on the concrete floor that might have increased the backscatter towards the radar and thus the RCS of the target.

There also was a light difference to be detected within the light rain measurement, but as the labels were very loose it was difficult to draw definite conclusions from this. Data from the light rain set either showed: no change at all, or a smaller change than in the heavy weather case. It was difficult to tell exactly what the difference was between these two cases.

Calibration coefficients estimation

At first two versions of estimation algorithms were introduced: one that estimates the full calibration matrix and one that estimates just the diagonal elements. They both operate on the same principle and require the angles of the targets to be known beforehand to create an ideal signal model. These angles do not need to be very precise to get an adequate estimation for the calibration coefficients. The algorithm finds the phase errors by finding the difference between the ideal signal model and real measurement data in a least-squares sense. It relates to the amplitude through the best performing antenna element.

Estimating the full set of calibration coefficients has the advantage that all mutual coupling terms are taken into account in the estimation, but perhaps this is not necessary for MIMO radar. Most of the errors are shown to be on the diagonal of the calibration matrix. Estimating only the diagonal elements is easier and adds stability to the estimation. Such an estimator also converges faster because it allows us to separate the problem and look at

each antenna element individually. This is why this algorithm is chosen be tracked in the Extended Kalman Filter.

The implementation of the Kalman filter shows that it is possible to track the calibration coefficients while driving. When the method converges it converges pretty quickly. It does not need a lot of measurements from targets to give a good estimation. This makes it useful for calibration on the go. The issues with stability have been avoided as much as possible, but this will still need some work before it will be fully functional. The algorithm is now ready to be used for radar purposes instead of for the application in robotics that it was mostly used for.

This was mainly achieved by removing the bearing from the state vector. To be able to do this it was necessary to make an estimator for the bearing that was related to the variables that are still being tracked in the algorithm. This was done using a weighted least squares estimator and it was needed to find an analytical expression that relates the variance of the real part of a random variable to the beam pointing error. This also gave an insight in the effect that phase errors have on the system and how the errors are distributed.

7.2. Future research

Adverse weather conditions

It will be important for future research to see if the observed effects were just because of a one-off scenario or show what can actually be observed in all types of scenarios. It might be that the observed effects were just because of the scenario on the roof in combination with the used radar and it would be useful to see if this can be seen other conditions.

If the effect can be seen in other scenarios and if there can be more data collected with accurate rainfall measurements it will be possible to create a new distribution model that describes the RCS shift of the target when it is raining. Studying the effect of the reflections on the detection of the target will improve the reliability of the radar in all weather conditions and road surfaces. To do this however more accurate rainfall rate data will be needed.

Calibration coefficients estimation

The goal is to constantly monitor how the radar is performing while driving and keep updating the calibration coefficients changes using objects of opportunity next to the road. The method that has been presented has shown that this is a possibility and that the proposed algorithm can be used for this purpose, but there is still room for improvement and for other research.

The initialisation of the calibration coefficients is especially important for the proposed technique: if the initialisation is entirely random then there is a chance that the algorithm will not converge to the right coefficients. Therefore it needs to be some kind of previous estimate of the calibration coefficients to go on. This might just be the estimate that came from the initial calibration when the radar comes out of the factory or estimations made in the previous set of measurements.

It might be useful to see how the algorithm performs when the data association is not perfect. The algorithm does not work well when targets are located too close together and this is why an imperfect data association might cause some errors.

Right now it is possible to calibrate the radar from objects of opportunity, but the method is not very robust right now. It is very reliant on the accuracy of the target measurements. When the deviations in the locations of the landmarks are too large then the the algorithm will draw the wrong conclusions and will not converge to the right coefficients.

One of the adjustments that still need to be made is to change the initialisation of new landmarks. Right now the algorithm is told on which side of the radar the landmarks will be and this is not ideal. To circumvent this it might be feasible to track all options at the same time and then decide which of the tracks is valid based on a hypothesis decision tree. The tracks would be assigned a probability and the amount of variance would be a good metric to see which track will be the right track.

The choice was made to only estimate the diagonal of the calibration matrix. It will be interesting to see if there is a solution to be found to include the whole calibration matrix with all mutual coupling coefficients. Perhaps there is a way to be found to track these coefficients in the Kalman filter or another implementation.

The next step for the calibration algorithm study can to apply it to real measurement data and see if it still will be able to perform a good calibration.

A

Equations for Extended Kalman Filter

A.1. Partial derivatives of Jacobian H

A.1.1. r

$$r = \sqrt{q} \tag{A.1}$$

$$\frac{\partial r}{\partial x} = \frac{-\sqrt{q}\delta_x}{q} \tag{A.2}$$

$$\frac{\partial r}{\partial y} = \frac{-\sqrt{q}\delta_y}{q} \tag{A.3}$$

$$\frac{\partial r}{\partial v} = 0 \tag{A.4}$$

$$\frac{\partial r}{\partial \theta} = 0 \tag{A.5}$$

$$\frac{\partial r}{\partial \gamma_m^R} = 0 \tag{A.6}$$

$$\frac{\partial r}{\partial \gamma_m^I} = 0 \tag{A.7}$$

$$\frac{\partial r}{\partial x_m} = \frac{\sqrt{q}\delta_x}{q} \tag{A.8}$$

$$\frac{\partial r}{\partial y_m} = \frac{\sqrt{q}\delta_y}{q} \tag{A.9}$$

A.1.2. v

$$v_R = v cos\phi \tag{A.10}$$

$$\phi = atan2(\delta_y, \delta_x) - \bar{\mu}_{R\theta} \tag{A.11}$$

$$\frac{\partial v_R}{\partial x} = -v sin\phi \frac{\delta_y}{q} \tag{A.12}$$

$$\frac{\partial v_R}{\partial y} = -v sin\phi \frac{\delta_x}{q} \tag{A.13}$$

$$\frac{\partial v_R}{\partial v} = cos\phi \tag{A.14}$$

$$\frac{\partial v_R}{\partial \theta} = vsin\phi \tag{A.15}$$

$$\frac{\partial v_R}{\partial \gamma_m^R} = 0 \tag{A.16}$$

$$\frac{\partial v_R}{\partial \gamma_m^I} = 0 \tag{A.17}$$

$$\frac{\partial v_R}{\partial x_m} = vsin\phi\frac{\delta_y}{q} \tag{A.18}$$

$$\frac{\partial v_R}{\partial y_m} = -vsin\phi\frac{\delta_x}{q} \tag{A.19}$$

A.1.3. gamma

$$P_m = \frac{X_m}{X_0} = \frac{\gamma_m}{\gamma_0}e^{j2\pi\frac{d}{\lambda}sin(\phi)m}, m = 1 \dots M-1 \tag{A.20}$$

$$\gamma_m = \frac{s_m x_m^H}{x_m x_m^H} \tag{A.21}$$

$$\psi = 2\pi\frac{d}{\lambda}sin\phi M \tag{A.22}$$

$$P_m = \gamma_m e^{j\psi_m} = \gamma_m(cos\psi_m + jsin\psi_m) \tag{A.23}$$

This is now split up in the real and imaginary parts: P_m^R and P_m^I.

$$P_m^R = Re(\gamma_m)cos\psi - Im(\gamma_m)sin\psi \tag{A.24}$$

$$P_m^I = Im(\gamma_m)sin\psi + Re(\gamma_m)sin\psi \tag{A.25}$$

Real parts

$$\frac{\partial P_m^R}{\partial x} = -Re(\gamma_m)sin\psi 2\pi\frac{d}{\lambda}cos\phi\frac{\delta_y}{q} \tag{A.26}$$

$$\frac{\partial P_m^R}{\partial y} = Re(\gamma_m)sin\psi 2\pi\frac{d}{\lambda}cos\phi\frac{\delta_x}{q} \tag{A.27}$$

$$\frac{\partial P_m^R}{\partial v} = 0 \tag{A.28}$$

$$\frac{\partial P_m^R}{\partial \theta} = Re(\gamma_m)sin\psi 2\pi\frac{d}{\lambda}cos\phi \tag{A.29}$$

$$\frac{\partial P_m^R}{\partial \gamma_m^R} = cos\psi \tag{A.30}$$

$$\frac{\partial P_m^R}{\partial \gamma_m^I} = -sin\psi \tag{A.31}$$

$$\frac{\partial P_m^R}{\partial x_m} = Re(\gamma_m)sin\psi 2\pi\frac{d}{\lambda}cos\phi\frac{\delta_y}{q} \tag{A.32}$$

$$\frac{\partial P_m^R}{\partial y_m} = -Re(\gamma_m)sin\psi 2\pi\frac{d}{\lambda}cos\phi\frac{\delta_x}{q} \tag{A.33}$$

Imaginary parts

$$\frac{\partial P_m^I}{\partial x} = Im(\gamma_m) sin\psi 2\pi \frac{d}{\lambda} cos\phi \frac{\delta_y}{q} \tag{A.34}$$

$$\frac{\partial P_m^I}{\partial y} = -Im(\gamma_m) sin\psi 2\pi \frac{d}{\lambda} cos\phi \frac{\delta_x}{q} \tag{A.35}$$

$$\frac{\partial P_m^I}{\partial v} = 0 \tag{A.36}$$

$$\frac{\partial P_m^I}{\partial \theta} = -Im(\gamma_m) sin\psi 2\pi \frac{d}{\lambda} cos\phi \tag{A.37}$$

$$\frac{\partial P_m^I}{\partial \gamma_m^R} = sin\psi \tag{A.38}$$

$$\frac{\partial P_m^I}{\partial \gamma_m^I} = cos\psi \tag{A.39}$$

$$\frac{\partial P_m^I}{\partial x_m} = -Im(\gamma_m) sin\psi 2\pi \frac{d}{\lambda} cos\phi \frac{\delta_y}{q} \tag{A.40}$$

$$\frac{\partial P_m^I}{\partial y_m} = Im(\gamma_m) sin\psi 2\pi \frac{d}{\lambda} cos\phi \frac{\delta_x}{q} \tag{A.41}$$

Bibliography

[1] Akram Al-Hourani, Robin J Evans, Peter M Farrell, Bill Moran, Marco Martorella, Sithamparanathan Kandeepan, Stan Skafidas, and Udaya Parampalli. Millimeter-wave integrated radar systems and techniques. In *Academic Press Library in Signal Processing, Volume 7*, pages 317–363. Elsevier, 2018.

[2] Benjamin T Arnold and Michael A Jensen. The effect of antenna mutual coupling on mimo radar system performance. *IEEE Transactions on Antennas and Propagation*, 67 (3):1410–1416, 2018.

[3] Tim Bailey and Hugh Durrant-Whyte. Simultaneous localization and mapping (slam): Part ii. *IEEE robotics & automation magazine*, 13(3):108–117, 2006.

[4] Francesco Belfiori, Wim van Rossum, and Peter Hoogeboom. Array calibration technique for a coherent mimo radar. In *2012 13th International Radar Symposium*, pages 122–125. IEEE, 2012.

[5] Kostadin G. Biserkov. Calibration procedure for mutual coupling of mimo radars. Extra student project, .

[6] K Carver, W Cooper, and W Stutzman. Beam-pointing errors of planar-phased arrays. *IEEE Transactions on Antennas and Propagation*, 21(2):199–202, 1973.

[7] Jonathon Y.C. Cheah. Wet antenna effect on vsat rain margin. *IEEE Transactions on Communications*, 41(8):1238–1244, 1993.

[8] N. Chen et al. The influence of the water-covered dielectric radome on 77ghz automotive radar signals. In *2017 European Radar Conference (EURAD)*, pages 139–142. IEEE, 2017.

[9] Continental. Continental standardized ars interface technical documentation ars 308. , Continental Engineering, 2011.

[10] Continental. Ars 30x/-2/-2c/-2t/-21 long range radar datasheet. , Continental Coorporation, 2012.

[11] Dahir H Dini and Danilo P Mandic. Class of widely linear complex kalman filters. *IEEE Transactions on Neural Networks and Learning Systems*, 23(5):775–786, 2012.

[12] Hugh Durrant-Whyte and Tim Bailey. Simultaneous localization and mapping: part i. *IEEE robotics & automation magazine*, 13(2):99–110, 2006.

[13] Michael Giallorenzo, Xiuzhang Cai, Adib Nashashibi, and Kamal Sarabandi. Radar backscatter measurements of road surfaces at 77 ghz. In *2018 IEEE International Symposium on Antennas and Propagation & USNC/URSI National Radio Science Meeting*, pages 2421–2422. IEEE, 2018.

[14] M. Harter, J. Hildebrandt, A. Ziroff, and T. Zwick. Self-calibration of a 3-d-digital beamforming radar system for automotive applications with installation behind automotive covers. *IEEE Transactions on Microwave Theory and Techniques*, 64(9):2994–3000, Sep. 2016.

[15] A.A. Hassen. *Indicators for the signal degradation and optimization of automotive radar sensors under adverse weather conditions*. Shaker Verlag, 2007.

[16] Eric Jacobsen and Peter Kootsookos. Fast, accurate frequency estimators [dsp tips & tricks]. *IEEE Signal Processing Magazine*, 24(3):123–125, 2007.

[17] Steven M Kay. *Fundamentals of statistical signal processing*. Prentice Hall PTR, 1993.

[18] Chevalier François Le. *Principles of radar and sonar signal processing*. Artech House, 2002.

[19] Eric S Li and Kamal Sarabandi. Low grazing incidence millimeter-wave scattering models and measurements for various road surfaces. *IEEE Transactions on Antennas and Propagation*, 47(5):851–861, 1999.

[20] Jian Li and Petre Stoica. *MIMO radar signal processing*, volume 7. Wiley Online Library, 2009.

[21] Robert J Mailloux. *Phased array antenna handbook*. Artech house, 2017.

[22] Marc Mowlér, Björn Lindmark, Erik G Larsson, and Björn Ottersten. Joint estimation of mutual coupling, element factor, and phase center in antenna arrays. *EURASIP Journal on Wireless Communications and Networking*, 2007(1):030684, 2007.

[23] V.W. Richard, J.E. Kammerer, and H.B. Wallace. Rain backscatter measurements at millimeter wavelengths. *IEEE transactions on geoscience and remote sensing*, 26(3):244–252, 1988.

[24] M.A. Richards et al. *Principles of modern radar*. Citeseer, 2010.

[25] F. Rosique, P.J. Navarro, C. Fernández, and A. Padilla. A systematic review of perception system and simulators for autonomous vehicles research. *Sensors*, 19(3):648, 2019.

[26] SandeepRao. Mimo radar application report. Technical report, Texas Instruments, 2018.

[27] Kamal Sarabandi, Eric S Li, and Abid Nashashibi. Modeling and measurements of scattering from road surfaces at millimeter-wave frequencies. *IEEE Transactions on Antennas and Propagation*, 45(11):1679–1688, 1997.

[28] C.M. Schmid et al. An fmcw mimo radar calibration and mutual coupling compensation approach. In *2013 European Radar Conference*, pages 13–16. IEEE, 2013.

[29] Roland Siegwart, Illah Reza Nourbakhsh, and Davide Scaramuzza. *Introduction to autonomous mobile robots*. MIT press, 2011.

[30] M.I. Skolnik. *The Radar handbook*. New York, McGraw-Hill, 1970.

[31] Hans Steyskal and Jeffrey S Herd. Mutual coupling compensation in small array antennas. *IEEE Transactions on Antennas and Propagation*, 38(12):1971–1975, 1990.

[32] Sebastian Thrun, Wolfram Burgard, and Dieter Fox. *Probabilistic robotics*. MIT press, 2005.

[33] VI Tikhonov. *Statistical radiotechnics*. , 1966. Book written in Russian.

[34] International Telecommunication Union. Recommendation itu-r p.838-3: Specific attenuation model for rain for use in prediction methods, 2005.